Water-wave-induced OBS noise: theories, observations and potential applications

Chun Zhang[1], **Chao An**[1]

[1]Key Laboratory of Hydrodynamics (Ministry of Education), School of Naval Architecture, Ocean and Civil Engineering, Shanghai Jiao Tong University, Shanghai, China.

Key Points:

- We propose a noise model to explain the horizontal OBS noise around 0.07 Hz in shallow water.
- The noise model and related theories are validated by realistic observations.
- Potential applications to determine water-wave direction, Earth structure inversion and noise removal are discussed.

Corresponding author: Chao An, anchao@sjtu.edu.cn

Abstract

The horizontal records of ocean-bottom seismometers (OBS) are usually highly noisy, generally due to ocean-bottom currents tilting the instrument, which greatly limits their practical usage in ocean-bottom seismology. In shallow water, water waves with energy concentration around 0.07 Hz induce additional noise on OBSs. Such noise is not well understood. In this article, we propose a noise model to explain the horizontal noise around 0.07 Hz. The noise model consists of three types of noise, that is, water-wave-induced noise, other noise with a relatively constant orientation, and background random noise. The wave-induced horizontal acceleration is theoretically shown to be proportional to the time derivative of ocean-bottom pressure. We validate the noise model and related theories using realistic observations. Results are potentially applicable to determine the propagation direction of water waves nearshore, and also provide constraints on the underlying Earth structure. The results can also be applied to the removal of wave-induced noise, achieving a typical maximum improvement in the signal-to-noise ratio of 10−20 dB for time periods with strong wave noise.

1 Introduction

Ocean-bottom seismometers (OBS) are deployed on the seafloor, mostly exposed to water, and hence they suffer from significant noise, particularly at low frequencies ($<$ 0.1 Hz). The noise level at OBS stations can be up to 40 dB higher compared to the quietest land stations (Peterson, 1993), which highly contaminate seismic signals from distant or weak earthquakes. The most well-known sources of low-frequency noise in OBS data are tilt noise and compliance noise (e.g., Webb, 1998; Crawford & Webb, 2000; Webb & Crawford, 2010).

Tilt noise is generally believed to originate from ocean-bottom currents which are typically driven by periodic tidal forces (e.g. Crawford & Webb, 2000; Bell et al., 2015; Reddy et al., 2020; Essing et al., 2021). Ocean-bottom currents pass around the instrument, causing turbulence and vortices, which tilt the instrument and generate noise in the horizontal channels (Sutton & Duennebier, 1987; Webb, 1988; Duennebier & Sutton, 1995; Romanowicz et al., 1998; Stähler et al., 2018). Tilt noise is generated through two mechanisms: the change of the seismometer's position and the change of the gravitational acceleration acting on the seismometer. For low frequencies, the second term dominates, and the horizontal noise is simply the production of the gravitational acceleration and the tilt angle (Crawford & Webb, 2000). Tilt noise in the horizontal channels can leak into the vertical due to imperfect leveling of the instrument. Using long-term recorded noise data, the tilt angle of the instrument can be calculated, and the tilt

noise in the vertical channel can be removed using the horizontal records (e.g., Crawford & Webb, 2000; Bell et al., 2015; An et al., 2020). The tilt noise in the horizontal channel is not well explained, except it is recently found that its orientation does not change in time (An et al., 2022), and the direction of maximum noise is probably perpendicular to the direction of bottom currents (Wu et al., 2023).

Another significant source of OBS noise is the water waves in the ocean. Long-period water waves can create ocean-bottom pressure variations and cause seafloor deformation, which is recorded by OBSs as compliance noise (e.g. Crawford et al., 1991; Crawford & Webb, 2000). According to the theoretical solution of a half-space elastic model, the vertical deformation is larger than the horizontal by roughly the square of the ratio of the compressional velocity to the shear velocity (Crawford, 2004). Thus, the term "compliance noise" commonly refers to the vertical compliance noise (e.g., Crawford et al., 1998; Crawford & Webb, 2000; Bell et al., 2015). Another reason is that the horizontal compliance noise is typically buried in other noise in the horizontal records such as tilt noise, and hence relevant studies are rare (Doran & Laske, 2016). A significant characteristic of compliance noise is the presence of different cut-off frequencies at different water depths. This phenomenon arises from the fact that the ability of water waves to penetrate the water and affect the seafloor depends on their wavelength, which is decided by their frequency, with a penetration depth of approximately one wavelength (e.g., Crawford et al., 1998; Crawford & Webb, 2000; Bell et al., 2015; An et al., 2020).

Current research on OBS noise mainly focuses on the vertical component and has made widely-accepted progress. Crawford & Webb (2000) first proposed that, since the vertical tilt noise is highly correlated to the horizontal tilt noise, one can calculate a transfer function between the vertical channel and the horizontal channel, and use the horizontal records to predict and remove the vertical tilt noise. A similar procedure can be adopted to remove the vertical compliance noise using a transfer function between the vertical and pressure channels. Bell et al. (2015) extended the idea by developing a model for the tilt noise which depends on the tilt angle and direction of the instrument. The technique of noise removal for the vertical records is applied to analyze ocean-bottom seismic data and study the Earth's structure (e.g., Wei et al., 2015; Bowden et al., 2016; Zha & Webb, 2016; Cai et al., 2018; Doran & Laske, 2019; Janiszewski et al., 2019). Besides, based on the mechanism of water waves deforming the elastic Earth, an inverse approach has been developed to constrain the Earth's elastic properties using recordings of vertical compliance noise and ocean-bottom pressure (e.g., Yamamoto & Torii, 1986; Crawford et al., 1998; Zha et al., 2014). A comprehensive summary on the understanding of OBS noise is given by Janiszewski et al. (2023).

The research on the horizontal noise is far less extensive compared to that on the vertical noise. In deep-sea environments, the primary source of low-frequency horizontal noise is the tilt noise. Understanding of the mechanism of the tilt noise has largely been qualitative, e.g., it is widely accepted that the tilt noise is associated with ocean-bottom currents (e.g., Duennebier et al., 1981; Trehu, 1985; Sutton & Duennebier, 1987; Webb, 1988; Duennebier & Sutton, 1995). An et al. (2022) analyzed in-situ observations and found that, the horizontal tilt noise has a principle noise direction which barely changes in time and may be related to the ocean-bottom current direction. An ideal denoise method is also not available. The use of vertical tilt noise to remove horizontal tilt noise is theoretically feasible, but it may cause significant signal distortion because the horizontal tilt noise is usually much larger than the vertical (e.g., An et al., 2020). An et al. (2022) proposes to rotate the horizontal records to the direction of the principle noise, so that the noise level in the orthogonal channel is reduced. However, the noise reduction is limited to one horizontal channel and a site-specific orientation. The horizontal compliance noise is usually much smaller than the tilt noise, but it can be identified in the horizontal records if the instrument is buried, and it is potentially useful to constrain the sedimentary and crustal structure by a joint inversion of vertical and horizontal compliance noise (Doran & Laske, 2016).

The horizontal noise in shallow waters (approximately $<$ 300 m) exhibits a distinctive characteristic: it has a strong peak between 0.05−0.1 Hz. Figure 1 shows the power spectral density (PSD) of the horizontal records at two OBS stations deployed in deep (3124 m) and shallow (93 m) water, respectively. The data are from the Cascadia Initiative (CI) (Toomey et al., 2014). It shows that the two PSD curves are similar below 0.04 Hz in that they are straight lines with a slope of about -1, which might be the feature of the tilt noise. However, between 0.05−0.1 Hz, the shallow PSD has a strong peak. It is inferred that the peak is caused by ocean-surface water waves, and the water waves with frequency around 0.07 Hz can only penetrate the shallow water column. In this article, we propose a noise model to explain the horizontal noise between 0.05−0.1 Hz, and then we derive the theory of water waves generating horizontal noise on OBSs. We validate the theory and noise model by comparing model predictions with realistic observations in section 3. Then we discuss potential applications of using the noise to infer water-wave propagation direction and constrain the underlying Earth structure, and develop methods to remove the noise.

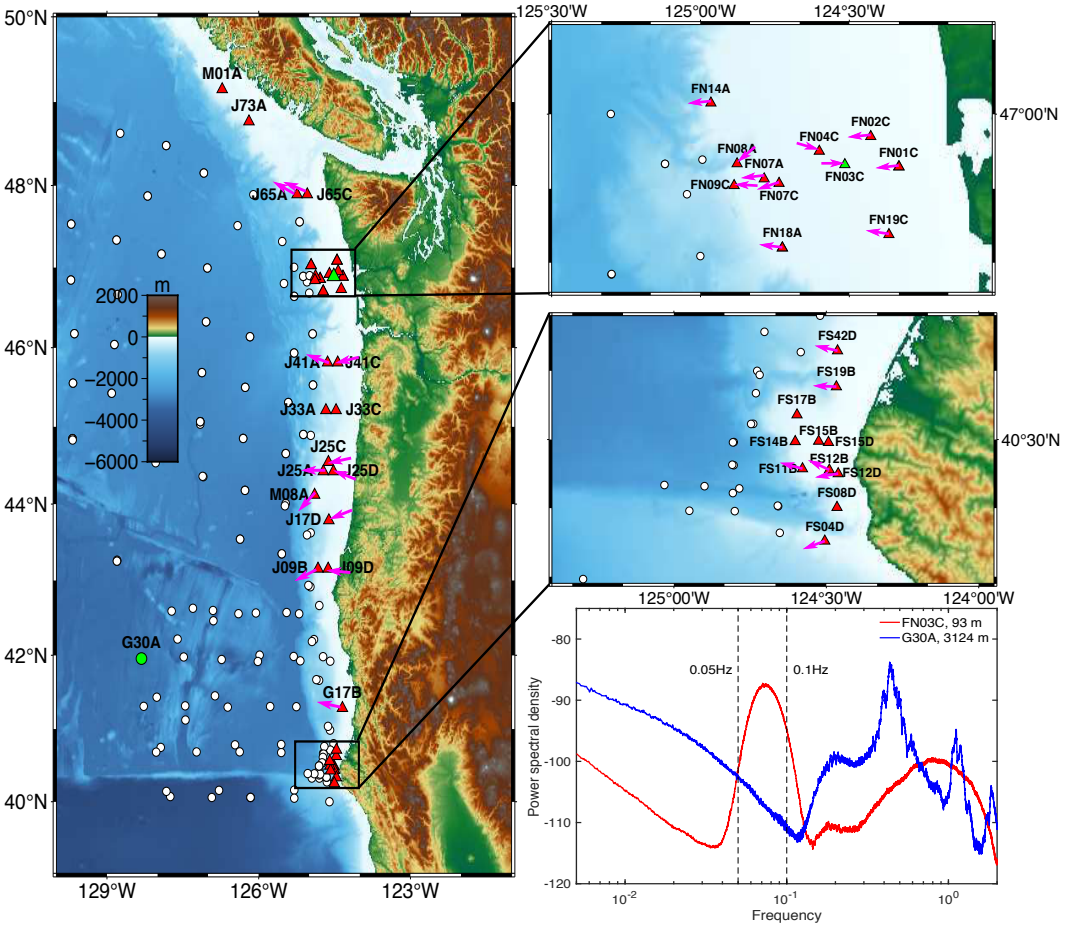

Figure 1. The location of the OBS stations from Cascadia Initiative. The triangles are the stations located in shallow water. The arrows represent the directions of water wave propagation inferred from the horizontal noise. The bottom right panel plots the power spectral density (PSD) at the shallow-water station FN03C and the deep-water station G30A. FN03C and G30A are marked in green in the map. A noise peak is observed around 0.07 Hz at FN03C, while no such phenomenon is observed at G30A.

2 Noise model and theory

2.1 Noise model

We propose a noise model to explain the horizontal OBS noise in shallow water around 0.07 Hz, shown in Figure 2. The model consists of three types of noise: wave noise $a_W(t)$, other noise $a_C(t)$ and background random noise $r(t)$. The wave noise is induced by ocean-surface water waves, and we will show that the instrumental measurement of such noise in acceleration is proportional to the time derivative of the ocean-bottom pressure. Other

noise is probably the current-induced noise, which has been widely observed in deep water, and its direction remains unchanged in time (An et al., 2022; Wu et al., 2023).

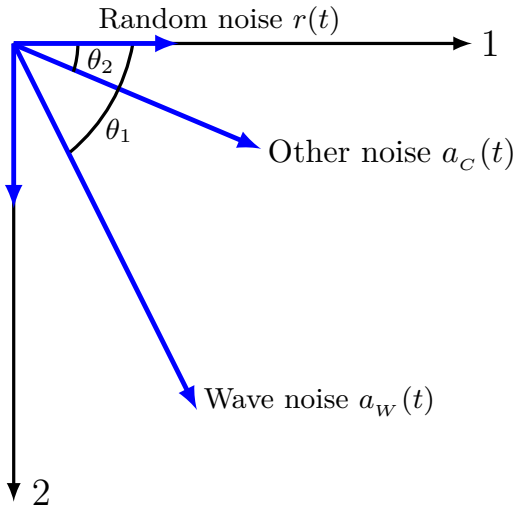

Figure 2. A model to explain the horizontal OBS noise in shallow water around 0.07 Hz. 1 and 2 denote the two horizontal channels of the instruments. Note that the recording coordinate system of the instrument is left-handed (Doran & Laske, 2017). $a_W(t)$, $a_C(t)$ and $r(t)$ represent wave noise, other noise and random noise, respectively. The wave noise and other noise are assumed to have constant orientations.

2.2 Noise induced by ocean-surface water waves: theory

Water waves generate noise on the OBS horizontal records through two mechanisms: by deforming the seafloor and by exerting wave forces on the instrument, respectively (Figure 3). Consider a sinusoidal water wave propagating on the ocean surface, such that the bottom pressure is written as

$$p(x,t) = p_0 e^{i(kx-\omega t)}, \tag{1}$$

in which p_0 is a constant, k and ω are the wave number and angular frequency of the wave, respectively. We can derive the response of the instrument analytically.

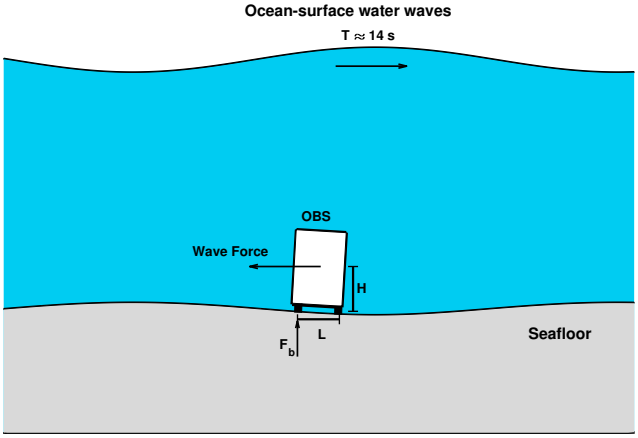

Figure 3. An OBS subject to water waves. Water waves generate horizontal noise by deforming the seafloor and by exerting wave forces on the instrument, respectively.

Under the loading of the ocean-bottom pressure, assuming a homogeneous half-space elastic media, the horizontal and vertical displacement of the seafloor is found to be (e.g., Crawford, 2004; An & Liu, 2016; An et al., 2020)

$$\begin{cases} U(x,t) = \dfrac{\beta^2}{\alpha^2-\beta^2}\dfrac{1}{2\mu k} i p_0 e^{i(kx-\omega t)}, & \text{(2a)} \\ W(x,t) = -\dfrac{\alpha^2}{\alpha^2-\beta^2}\dfrac{1}{2\mu k} p_0 e^{i(kx-\omega t)}. & \text{(2b)} \end{cases}$$

Here α and β are the P- and S-wave velocities, respectively, and μ is the shear modulus of the Earth. Note that we have assumed the water-wave speed is much smaller than that of the seismic waves, that is, $\omega^2/k^2 \ll \alpha^2$ and $\omega^2/k^2 \ll \beta^2$. The apparent acceleration of the OBS consists of two parts: the horizontal acceleration of the seafloor, $\mathrm{d}^2U/\mathrm{d}t^2$, and the tilting of the seafloor which causes leaking of the gravitational acceleration into the horizontal channel. They are calculated as follows.

$$\begin{cases} a_{\mathrm{def}} = \dfrac{\mathrm{d}^2U}{\mathrm{d}t^2} = \dfrac{\beta^2}{\alpha^2-\beta^2}\dfrac{\omega}{2\mu k}\dfrac{\mathrm{d}p}{\mathrm{d}t}, & \text{(3a)} \\ a_{\mathrm{tilt}} = -g\dfrac{\mathrm{d}W}{\mathrm{d}x} = -\dfrac{\alpha^2}{\alpha^2-\beta^2}\dfrac{g}{2\mu\omega}\dfrac{\mathrm{d}p}{\mathrm{d}t}. & \text{(3b)} \end{cases}$$

Note that a_{tilt} is the product of gravitational acceleration and the instrumental tilting angle for low frequencies (Crawford & Webb, 2000), and the tilting angle of the seafloor is approximated by $\mathrm{d}W/\mathrm{d}x$ due to its small value. We emphasize that the above theory is not new, but has been proposed in previous studies (e.g., Crawford, 2004; Araki et al.,

2004; Webb & Crawford, 2010; Doran & Laske, 2016). The ratio of the two is estimated to be

$$\frac{a_{\text{def}}}{a_{\text{tilt}}} = -\frac{\beta^2}{\alpha^2}\frac{\omega^2}{gk} = -\frac{\beta^2}{\alpha^2}\tanh kh. \tag{4}$$

Here we have used the dispersion relationship for water waves, that is, $\omega^2 = gk\tanh kh$ (h water depth). Supposing $\beta^2 \approx 1/3\,\alpha^2$ and considering $\tanh kh < 1$, it is inferred that a_{def} is smaller than a_{tilt}, but it is non-negligible unless the wavelength of the water wave is much larger than the water depth ($kh \ll 1$).

A wave exerts two kinds of forces on an object submerged in fluid: the drag force F_{drag} which is proportional to the square of fluid velocity, and the inertia force F_{iner} which is proportional to fluid acceleration:

$$\begin{cases} F_{\text{drag}} = \dfrac{1}{2}C_D\,\rho S v|v|, & \text{(5a)} \\ F_{\text{iner}} = \big(1+k_m\big)\rho V\dfrac{\mathrm{d}v}{\mathrm{d}t}. & \text{(5b)} \end{cases}$$

Here C_D is the drag coefficient, ρ is the fluid density, v is the fluid velocity, S is the projected area in the wave direction, V is the object volume, and k_m is the coefficient of added mass which depends on the object shape. Refer to Chapter 8 of Dalrymple & Dean (1991) for more details. The ratio of the drag force and the inertia force, called the K_C number, is estimated approximately as

$$K_C = \frac{F_{\text{drag}}}{F_{\text{iner}}} \approx \frac{v\,T}{l} \approx \frac{A}{l}, \tag{6}$$

in which T is the wave period, A is the wave amplitude and l is the object size. For small-amplitude water waves, K_C is small, and it is reasonable to ignore the drag force. A force acting on the instrument causes the instrument to tilt, and the tilting angle is linearly proportional to the force (Webb, 1988). The instrumental record is the product of the gravitational acceleration and the tilting angle, that is,

$$a_{\text{iner}} = CF_{\text{iner}}\,g = Cg\big(1+k_m\big)\rho V\frac{\mathrm{d}v}{\mathrm{d}t} = Cg\big(1+k_m\big)V\frac{k}{\omega}\frac{\mathrm{d}p}{\mathrm{d}t}. \tag{7}$$

Here C is a constant depending on the elastic properties of the Earth and the configuration of the instrument, and CF_{iner} represents the tilting angle of the instrument. Note that in deriving the above equation, we have used a relationship between the ocean-bottom pressure and fluid velocity for water waves, that is, $p = \rho\,v\,\omega/k$ (Dalrymple & Dean, 1991, their chapter 3).

Combining equations (3a), (3b) and (7), and using equation (1), the wave-induced apparent OBS acceleration is

$$a_{_W} = a_{\rm def} + a_{\rm tilt} + a_{\rm iner} = \left[\frac{\beta^2}{\alpha^2-\beta^2}\frac{\omega}{2\mu k} - \frac{\alpha^2}{\alpha^2-\beta^2}\frac{g}{2\mu\omega} + Cg\big(1+k_m\big)V\frac{k}{\omega}\right]\frac{{\rm d}p}{{\rm d}t}. \quad (8)$$

Equation (8) indicates that the wave-induced OBS record is linearly proportional to the time derivative of the bottom pressure, and we define the coefficient as K. Using the dispersion relationship of water waves, that is, $\omega^2 = gk\tanh(kh)$, we rewrite the coefficient K as a function of kh:

$$K = -\frac{1}{2\mu}\frac{\alpha^2}{\alpha^2-\beta^2}\frac{\sqrt{gh}}{\sqrt{kh\,\tanh kh}}\left(-\frac{\beta^2}{\alpha^2}\tanh kh + 1\right) + C\big(1+k_m\big)V\sqrt{\frac{g}{h}}\frac{\sqrt{kh}}{\sqrt{\tanh kh}}. \quad (9)$$

So $a_{_W} = K{\rm d}p/{\rm d}t$. Note that the first term in this equation is negative, and the second term is positive, so the sign of K depends on the relative importance of the two mechanisms. We point out that the above relationship is obtained based on the assumption of uniform half-space elastic model. For layered structures of the real Earth, the dependence of K on kh will be more complicated, but $a_{_W}$ is still proportional to ${\rm d}p/{\rm d}t$.

2.3 Relative importance of seafloor tilt and wave inertia force

Here we provide a rough estimation of the relative importance of the seafloor tilting and wave inertia force on generating OBS apparent acceleration. We assume that the OBS is a cylinder in contact with the seafloor through foot pads (Figure 3), and we can estimate the coefficient C in equation (7). Due to the wave force $F_{\rm iner}$ acting on the instrument, a supporting force F_b provided by the ground is required to balance the torque, and $F_b\,L = F_{\rm iner}\,H$. The vertical displacement of the ground caused by F_b, denoted by Δz, can be calculated by integrating the solution of the Boussinesq problem over the foot pad (e.g., Webb, 1988):

$$\Delta z = \frac{2F_b}{\pi R}\frac{1-\nu^2}{E} = \frac{2H}{\pi RL}\frac{1-\nu^2}{E}(1+k_m)\rho V\frac{k}{\rho\,\omega}\frac{{\rm d}p}{{\rm d}t}, \quad (10)$$

in which E and ν are the Young's modulus and Poisson's ratio of the Earth. The tilting angle of the instrument is simply $\Delta z/L$. So the apparent acceleration recorded by the OBS is

$$a_{\rm iner} = g\frac{\Delta z}{L} = \frac{2H}{\pi RL^2}\frac{1-\nu^2}{E}(1+k_m)\rho g V\frac{k}{\rho\,\omega}\frac{{\rm d}p}{{\rm d}t}. \quad (11)$$

Using equation (3b), the ratio of $a_{\rm iner}$ and $a_{\rm tilt}$ is estimated to be

$$\frac{a_{\rm iner}}{a_{\rm tilt}} = -\left(1-\frac{\beta^2}{\alpha^2}\right)\big(1-\nu\big)\big(1+k_m\big)\frac{H}{R}\frac{H}{\lambda}. \quad (12)$$

Here λ is the wavelength of the water wave ($\lambda = 2\pi/k$). Equation (12) indicates that the relative importance of the seafloor tilting and the wave force depends on H/R and

H/λ, which are the ratio of the instrument size to the foot pad size, and the ratio of instrument size to the water wave wavelength, respectively. For general instrumental settings, $H/R > 1$ and $H/\lambda < 1$. Therefore, the two mechanisms can be equally important. Furthermore, since a_{iner} and a_{tilt} have different signs, the sign of the total apparent acceleration a_W will depend on which of the two is relatively larger.

3 Model Validation by realistic observations

3.1 Model validation

According to the proposed noise model in Figure 2, there are five model parameters, $a_W(t)$, $a_C(t)$, $r(t)$, θ_1 and θ_2. For realistic recordings, we will derive these parameters by rotating the data in the horizontal plane. First, the two original horizontal records are denoted as

$$\begin{cases} a_1(t) = a_W(t)\cos\theta_1 + a_C(t)\cos\theta_2 + r(t), & \text{(13a)} \\ a_2(t) = a_W(t)\sin\theta_1 + a_C(t)\sin\theta_2 + r(t). & \text{(13b)} \end{cases}$$

Rotating the records clockwise by an arbitrary angle δ, channel 1 will be

$$a_1(\delta) = a_W(t)\cos\left(\theta_1 - \delta\right) + a_C(t)\cos\left(\theta_2 - \delta\right) + r(t). \tag{14}$$

We define the averaged amplitude of the rotated data and its correlation with $\mathrm{d}p/\mathrm{d}t$ as

$$\begin{cases} \Gamma_{11}(\delta) = \sqrt{\dfrac{1}{t_1}\displaystyle\int_0^{t_1} a_1^2 \mathrm{d}t} = \sqrt{\left|a_W\right|^2\cos^2\left(\theta_1-\delta\right) + \left|a_C\right|^2\cos^2(\theta_2-\delta) + \left|r\right|^2}, & \text{(15a)} \\ \gamma_{1p}(\delta) = \left| \dfrac{\int_0^{t_1} a_1 \frac{\mathrm{d}p}{\mathrm{d}t}\mathrm{d}t}{\sqrt{\int_0^{t_1} a_1^2 \mathrm{d}t}\,\sqrt{\int_0^{t_1}\left(\frac{\mathrm{d}p}{\mathrm{d}t}\right)^2\mathrm{d}t}} \right| = \sqrt{\dfrac{\left|a_W\right|^2\cos^2(\theta_1-\delta)}{\left|a_W\right|^2\cos^2(\theta_1-\delta) + \left|a_C\right|^2\cos^2(\theta_2-\delta) + \left|r\right|^2}}, & \text{(15b)} \end{cases}$$

in which t_1 is an arbitrary time length that is long enough to calculate the average, and

$$\left|a_W\right| = \sqrt{\frac{1}{t_1}\int_0^{t_1} a_W^2 \mathrm{d}t}, \quad \left|a_C\right| = \sqrt{\frac{1}{t_1}\int_0^{t_1} a_C^2 \mathrm{d}t}, \quad \left|r\right| = \sqrt{\frac{1}{t_1}\int_0^{t_1} r^2 \mathrm{d}t}, \tag{16}$$

representing the averaged amplitude of wave noise, other noise and background random noise. Note that here we have assumed

$$\int_0^{t_1} a_W a_C \mathrm{d}t = 0, \quad \int_0^{t_1} a_W r\,\mathrm{d}t = 0, \quad \text{and} \quad \int_0^{t_1} a_C r\,\mathrm{d}t = 0. \tag{17}$$

We have also used $a_W = K\mathrm{d}p/\mathrm{d}t$ (equation 8).

For realistic recordings, we will use Γ_{11} and γ_{1p} to calculate the five model parameters. We first filter the noise data between 0.05−0.1 Hz, and then cut the continuous time series into small segments of length 1,000 s. For each segment, we rotate the data by five arbitrary angles, $\delta_1 - \delta_5$. For $\delta_1 - \delta_3$, we calculate the average noise amplitude, Γ_{11}; for δ_4 and δ_5, we calculate the correlation, γ_{1p}. Then according to equation (15), and we can solve for the five unknowns $|a_W|$, $|a_C|$, $|r|$, θ_1 and θ_2. We point out that the five δ angles are arbitrary, and the results are robust regardless of the choice of the rotating angle. We also note that the choice of calculating Γ_{11} or γ_{1p} does not affect the results, as long as the five obtained equations are independent. An example of the calculated model parameters is shown in Figure 4. It is interesting to observe that the amplitude of the noise is larger from October to May, which could be attributed to seasonal effects leading to strong water waves during this period. Many other stations also show similar trends. The results of the five model parameters at all the 37 stations are shown in Figure S1 in the supplementary information.

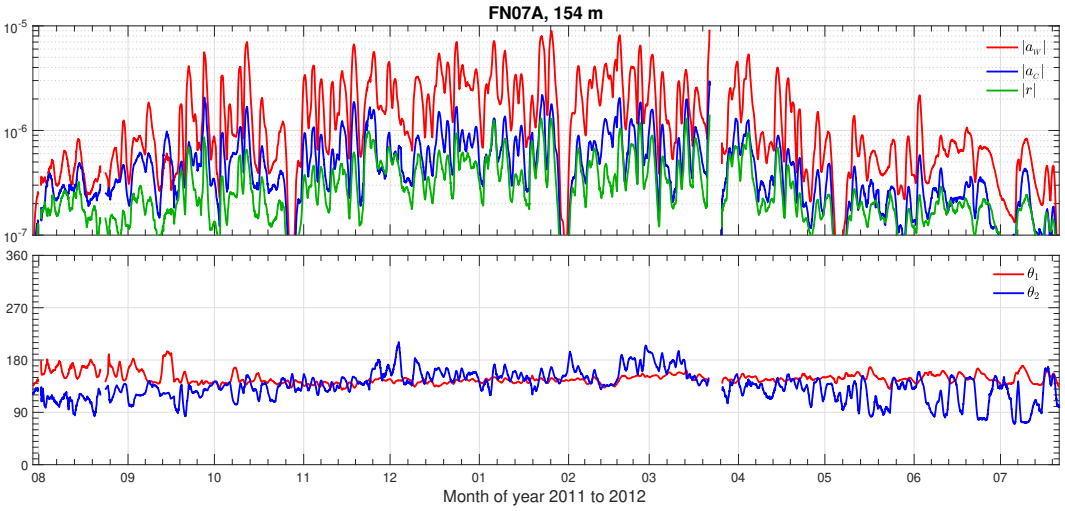

Figure 4. The five model parameters $|a_W|$, $|a_C|$, $|r|$, θ_1 and θ_2 obtained at station FN07A. The results are presented after a moving average using a 10-hour duration.

To validate the noise model, we use the five parameters to predict some noise properties, and then compare the predictions with realistic calculations. Here we choose two special angles for the validation, that is, the rotating angles to minimize and maximize the correlation between channel 1 and $\mathrm{d}p/\mathrm{d}t$. According to equation (15b), the noise model predicts that the two angles to minimize and maximize γ_{1p} are

$$\begin{cases} \delta_{1p_{\min}} = \theta_1 + \dfrac{\pi}{2} + n\pi & \text{(18a)} \\ \delta_{1p_{\max}} = \theta_2 + \chi + n\pi, \quad \chi = \arctan\left[\dfrac{|a_C|^2 + |r|^2}{|r|^2}\tan(\theta_1 - \theta_2)\right]. & \text{(18b)} \end{cases}$$

For realistic recordings, we rotate the data continuously from 0 to 180° with an interval of 1° to find the minimum and maximum correlation between channel 1 and dp/dt. Figure 5 shows the comparison at station FN07A. It is seen that a perfect agreement is obtained between the model-predicted angles and angles from rotation of realistic data. This demonstrates that our model well represents the noise characteristics of realistic observations. We point out that this validation process is performed for all the stations used in this study, and the results are similar.

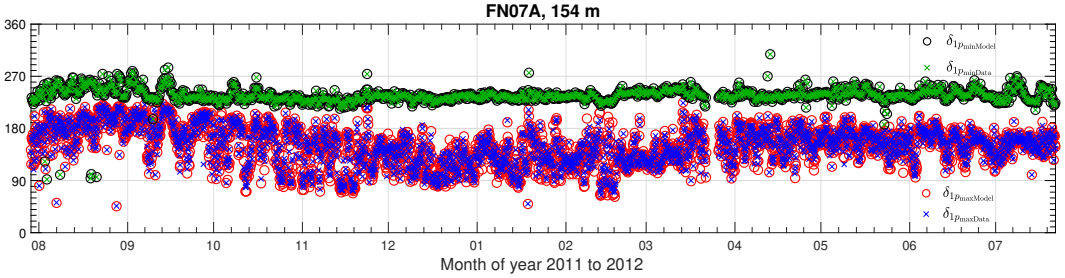

Figure 5. The rotating angles to minimize and maximize the correlation between channel 1 and dp/dt: model predictions and calculations from realistic data. The perfect agreement indicates that our noise model agrees well with the real noise recordings.

3.2 Necessity of other noise and random noise

Figure 4 already shows that $|a_C|$ and $|r|$ are non-negligible compared to $|a_W|$. Here we show more evidence to prove that other noise and random noise are necessary to explain the real data.

Equation (18b) suggests that, if $|a_C| = 0$, $\delta_{1p_{\max}} = \theta_1$, which means that if other noise is absent, the angle to maximize the correlation between channel 1 and dp/dt is simply the direction of the wave noise. In contrast, if other noise is non-negligible, $\delta_{1p_{\max}}$ deviates from θ_1. Figure 6(a) shows that the two angles are different at FN07A. At many other stations, we also observe that such an angle difference is clear and significant (Figure S1). Supposing that other noise is caused by an ocean-bottom current, it indicates that the bottom current is non-negligible, and its direction is not the same as or perpendicular to the propagation direction of ocean-surface water waves.

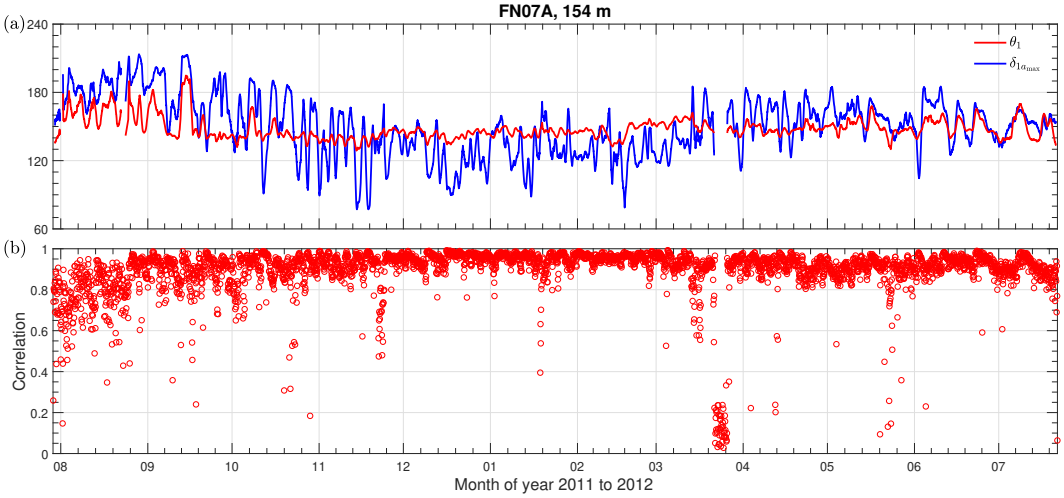

Figure 6. (a) θ_1 and $\delta_{1p_{\max}}$ obtained at FN07A. Significant differences can be observed between them, indicating that other noise is non-negligible in real data. (b) The maximum correlation between channel 1 and dp/dt. The results remain below 1, indicating the necessity of background random noise.

The necessity of random background noise is related to the maximum correlation between channel 1 and dp/dt. According to equation (15b), in the absence of random noise, $|r| = 0$, and the maximum value of γ_{1p} is 1 when $\delta = \theta_2 + \pi/2$. This is intuitive, because rotating the recordings to the perpendicular direction of other noise will totally eliminate other noise, resulting in only the component of wave noise, that is, $a_1 = a_W \sin(\theta_2 - \theta_1)$ (equation 14). Thus, the correlation between a_1 and dp/dt will be 1, given that $a_W = K$dp/dt. However, for most stations, we observe that the maximum correlation between channel 1 and dp/dt is less than 1 (Figure 6b, Figure S1), indicating the necessity of random background noise in the model.

3.3 Linear dependence of the wave noise on dp/dt

The noise model in Figure 2 suggests mathematically that, for horizontal OBS noise in shallow water around 0.07 Hz, there is a noise component that is proportional to dp/dt. In previous sections, we have shown that it is possible to decompose the real data and obtain the relative amplitude of such a component, that is, $|a_W|$. Here we show more quantitative evidence using the noise waveforms.

We select station FN03C to illustrate the linear relationship between a_W and dp/dt. The water depth at FN03C is 93 m, and the location of station FN03C is highlighted in green in Figure 1. The horizontal recordings are filtered between $0.05 - 0.1$ Hz and

cut into segments of 1,000 s. For each segment, we rotate the data by five arbitrary angles, and calculate the five model parameters. Two of the model parameters, θ_1 and θ_2, are shown in are shown in Figure 7(a). Figure 7(a) shows the reason to choose station FN03C, that is, the wave noise is approximately perpendicular to other noise. Thus, rotating the data clockwise by θ_1 will completely eliminate other noise, and only the wave noise and random noise are left. Figure 7(b) plots the correlation between channel 1 and $\mathrm{d}p/\mathrm{d}t$ after rotating the data to the direction of wave noise. It is seen that the correlation coefficient is very close to 1, indicating high similarity of channel 1 and $\mathrm{d}p/\mathrm{d}t$. We also examine the waveforms. We randomly choose one data segment to show in Figure 7(c). A perfect match is observed between the noise waveform of channel 1 and $\mathrm{d}p/\mathrm{d}t$, which is in agreement with our theory of wave-induced noise. The factor between the two, that is, the coefficient K in equation (9), is not quantitatively explained here since it depends on unknown properties such as the instrumental size and the Earth's elastic parameters.

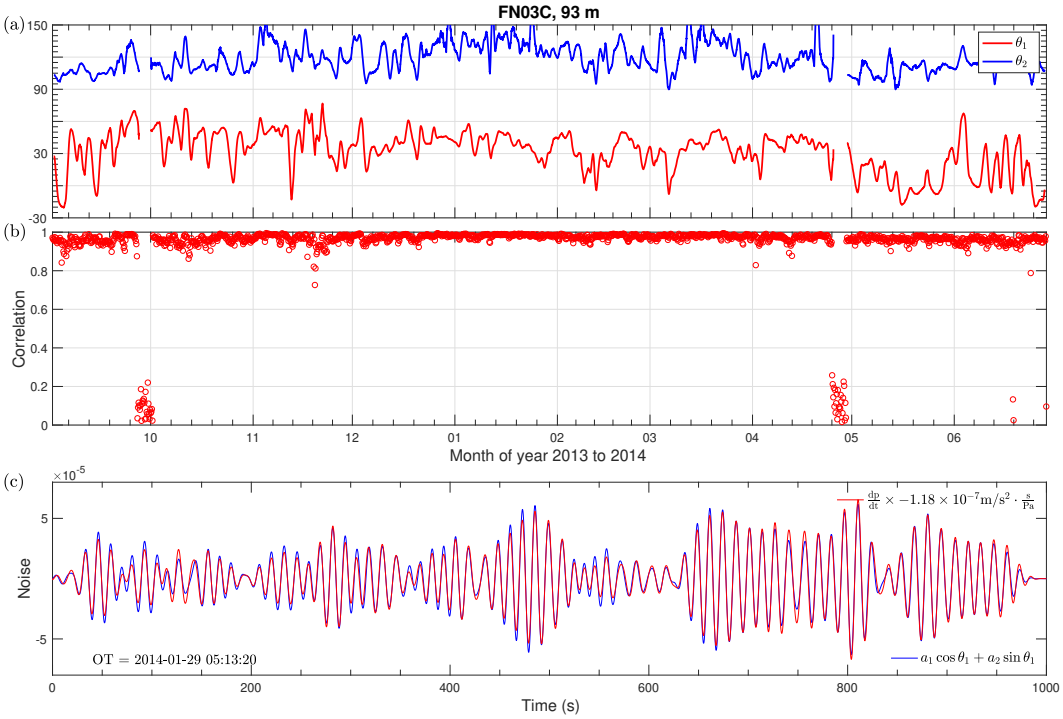

Figure 7. (a) The direction of wave noise and other noise at station FN03C. The two directions are approximately perpendicular. (b) The correlation between channel 1 and $\mathrm{d}p/\mathrm{d}t$ after rotating the data by θ_1. The correlation is very close to 1, indicating that the random noise is small and there exists high similarity between channel 1 and $\mathrm{d}p/\mathrm{d}t$. (c) Waveform comparison of a randomly selected segment. Channel 1 after rotation is proportional to $\mathrm{d}p/\mathrm{d}t$.

4 Potential applications

4.1 The propagation direction of water waves

In the previous sections, we have shown that we can determine five model parameters from real data, that is, $|a_{W}|$, $|a_{C}|$, $|r|$, θ_1 and θ_2. Here θ_1 simply represents the propagation direction of water waves. However, the propagation can also be opposite, because the sign of the K coefficient is uncertain (equation 9). K can be positive or negative depending on the relative importance of seafloor deformation and wave force in generating the wave noise. In this section, we illustrate a procedure to determine the real wave direction based on K's frequency dependence.

We first rewrite $a_{W} = K\mathrm{d}p/\mathrm{d}t$ using the vertical acceleration a_{v} instead of the pressure p. The reason is that realistic measurements of p often use differential pressure gauges (DPG), which suffer from amplitude uncertainties and possible polarity errors (e.g., Sheehan et al., 2015; Zha & Webb, 2016; Doran et al., 2019; An et al., 2020). Thus the pressure data are not directly applicable unless they are calibrated (e.g., An et al., 2017; Deng et al., 2022). Based on the uniform half-space elastic theory, according to equation (2b), the vertical acceleration is found to be

$$a_{v} = \frac{\alpha^2}{\alpha^2 - \beta^2} \frac{\omega^2}{2\mu k}\, p. \tag{19}$$

Replacing p by a_{v} in equation $a_{W} = K\mathrm{d}p/\mathrm{d}t$, we obtain a new parameter K^*, which is defined by

$$a_{W} = K \frac{\mathrm{d}p}{\mathrm{d}t} = K^* \frac{\mathrm{d}a_{v}}{\mathrm{d}t}. \tag{20}$$

Using equation (9), K^* is expressed as

$$K^* = -K_1^* + K_2^* = -\sqrt{\frac{h}{g}} \sqrt{\frac{1}{kh\,(\tanh kh)^3}} \left(-\frac{\beta^2}{\alpha^2} \tanh kh + 1 \right) + C_2 \sqrt{\frac{kh}{(\tanh kh)^3}}. \tag{21}$$

Note that the k-independent coefficient in the second term is written as a positive constants C_2 for simplicity, and

$$C_2 = C\big(1 + k_m\big) V \left(1 - \frac{\beta^2}{\alpha^2} \right) \frac{2\mu}{\sqrt{gh}}. \tag{22}$$

K_1^* and K_2^* are both positive, but their relative importance is not known, so the sign of K^* is uncertain. Here we determine the wave direction based the dependence of

K^* on kh. For reasonable value range of β/α and kh, it is found that K_1^* decreases monotonically with kh, while K_2^* increases monotonically with kh (see Figure S2 in the supplementary information). Thus, the behavior of K^* on kh can be predicted as shown in Table 1. If the measuring direction of the instrument is the opposite to the wave propagation direction (possibilities 3 and 4 in Table 1), the calculated K^* will be also opposite to equation (21). Thus, the sign of calculated K^* not only depends on the measuring direction, but also the relative size of K_1^* and K_2^*. However, the monotonicity of the calculated K^* on kh depends only on the measuring direction. Thus, the direction of the wave propagation can be determined based on K^*'s monotonicity dependence on kh.

Table 1. The behavior of apparent K^* on kh.

Possibility	Measuring Direction	K_1^* and K_2^*	Sign of K^*	Monotonicity on kh
1	Wave Direction	$K_1^* > K_2^*$	$-$	$\nearrow$
2	Wave Direction	$K_1^* < K_2^*$	$+$	$\nearrow$
3	Opposite	$K_1^* > K_2^*$	$+$	$\searrow$
4	Opposite	$K_1^* < K_2^*$	$-$	$\searrow$

The detailed procedure is explained as follows. We first filter the data between a narrow frequency band with a 0.01 Hz interval. For each frequency band, we cut the continuous data into small segments of 1,000 s, and calculate the five model parameters. Then, we rotate each data segment clockwise by the angle of $\theta_2 \pm \pi/2$, which is the perpendicular direction of other noise, so that other noise is completely eliminated. Then we calculate K^* using a least square method to minimize the residual between a_1 and $K^* \mathrm{d}a_v/\mathrm{d}t$. Based on the monotonicity of K^* on kh, we can determine the direction of water wave propagation. An example is shown in Figure 8. Figure 8(a) plots θ_1, and Figure 8(b) plots the calculated K^* after rotating the data. It is seen that K^* increases as kh increases, so the measuring direction is the same as the wave propagation direction, corresponding to possibilities 1 and 2 in Table 1. We point out that Figure 8(b) uses frequency instead of kh for illustration. For water waves, the frequency f and kh are linked by the dispersion relationship $\omega^2 = gk \tanh kh$, and since the water depth is constant, they are actually equivalent.

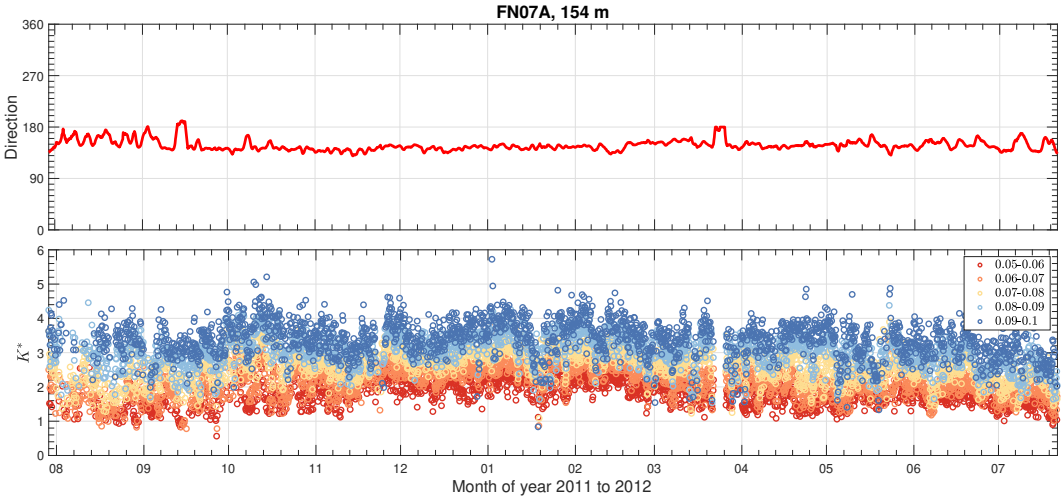

Figure 8. (a) Angle of θ_1 at station FN07A. (b) Calculated K^* in different frequency ranges at FN07A. Since K^* increases as kh (or frequency) increases, it is inferred that the direction of θ_1 is the same as the propagation direction of water waves.

The obtained angle of wave propagation is the deviated angle from channel 1, and it must be added to the orientation of the instrument to derive the real wave direction. Here we use the results of instrumental orientation given by Doran & Laske (2017). At some stations the instrumental orientation has high uncertainties, and we discard these stations. We also exclude the stations with unclear monotonic relationships of K^* on kh. The final results are displayed in Figure 1. The results show that, at all the 27 stations we have analyzed, the wave propagation direction is always perpendicular to the coastline. Among them, at 25 stations the waves propagate from shallow water to deep sea. This may indicate that the water waves are possibly the infragravity waves which are generated in the shallow region and leaked into the deep ocean (e.g, Herbers et al., 1995). Stations FN03C and FN04C present opposite wave directions, that is, water waves propagate towards the coastline. One possible reason could be the uniform half-space elastic assumption we have made in the analysis. Real Earth has layered structures, which leads to different dependence of K^* on kh, causing uncertainties in determining the water wave direction. However, we point out that even at these two stations, the angle of θ_1 is accurately calculated, and the uncertainty is only a 180-degree difference.

4.2 Inversion of subsurface structure

Based on the above-developed theory, it is possible to utilize the wave noise to constrain the subsurface Earth structure. Here we first discuss the situation in which ocean-

bottom pressure data are not available, that is, either a pressure sensor is missing or the pressure data are not calibrated. We will utilize the horizontal and vertical acceleration to perform the inversion. We first rotate the data to the perpendicular direction of other noise to totally eliminate other noise. According to equation (14), using a_1 and a_2 to denote the original horizontal records, letting the rotating angle $\delta = \theta_2 + \pi/2$, and ignoring the background random noise, we obtain

$$a_W = \frac{-a_1 \sin\theta_2 + a_2 \cos\theta_2}{\sin\left(\theta_1 - \theta_2\right)}. \tag{23}$$

Using equations (20) and (21), we have

$$\frac{-a_1 \sin\theta_2 + a_2 \cos\theta_2}{\sin\left(\theta_1 - \theta_2\right)} \Big/ \frac{\mathrm{d}a_v}{\mathrm{d}t} = -\sqrt{\frac{h}{g}} \sqrt{\frac{1}{kh\left(\tanh kh\right)^3}} \left(-\frac{\beta^2}{\alpha^2}\tanh kh + 1\right) + C_2 \sqrt{\frac{kh}{(\tanh kh)^3}}. \tag{24}$$

The equation essentially means that the horizontal acceleration after rotation is linearly proportional to the time derivative of the vertical acceleration, and the coefficient K^*, is a function of kh, β/α and C_2. For realistic recordings, we first cut the continuous data into segments of 1000 s and derive the five model parameters. Then we calculate the left-hand side of equation (24), and perform a least-square search to find β/α and C_2 of the best match. An example is shown in Figure 9.

For each time segment, we calculate K^* as a function of kh. Again here kh is equivalent to the frequency f according to the wave dispersion relationship $\omega^2 = gk\tanh kh$. All the results of K^* are stacked and displayed as a contour plot in Figure 9(a). The white line in Figure 9(a) shows the best fit of the inversion, and β^2/α^2 and C_2 are found to be 0.84 and 1.6 respectively. We also test the stability of the inversion. Figure 9(b) shows the contour plot of the inversion residual. It is observed that there is a clear trade-off between the two inversion parameters β^2/α^2 and C_2.

The best result of β^2/α^2 is calculated to be 0.84 in our inversion, which is higher than that of an elastic rock with the Possion's ratio 0.25 ($\beta^2/\alpha^2 = 1/3$). This may be attributed to the uniform half-space model we have assumed in the analysis. Real Earth has layered structures. For layered models, in equation (24), the first term on the right-hand side can be calculated using a numerical or propagation-matrix approach, leading to a different dependence on kh, while the second term does not change. Therefore, the inversion parameters are still β/α and C_2 for layered models. The sensitivity and uncertainties of this method should be discussed in a more detailed manner in future studies.

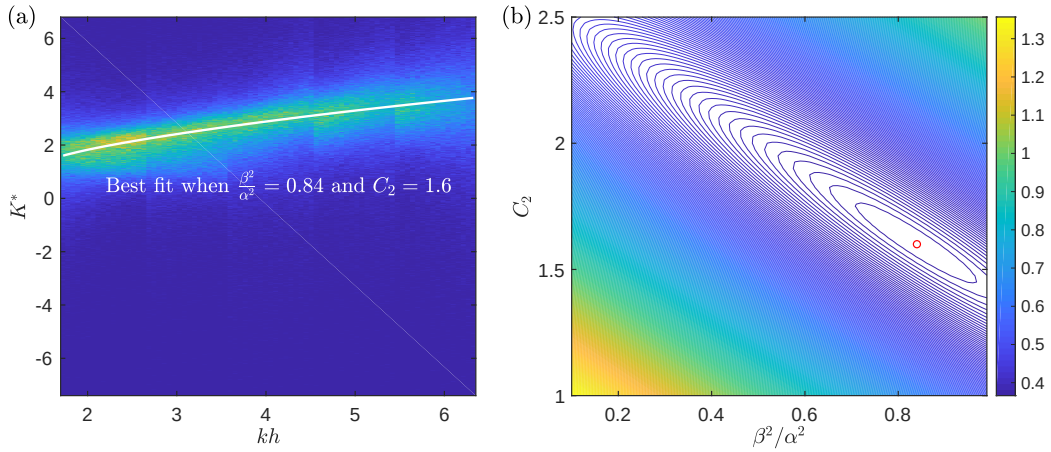

Figure 9. (a) Stacked K^* as a function of kh and its best fit to constrain β^2/α^2 and C_2. (b) Contour plot of the inversion residual. It is seen that there is a trade-off between the inversion parameters β^2/α^2 and C_2.

If the pressure records are available, it is possible to perform a joint inversion using the horizontal and vertical acceleration and the pressure. For a uniform half-space model, the equations have been derived in (8), (9) and (19). They are repeated as follows.

$$\begin{cases} \dfrac{-a_1 \sin\theta_2 + a_2 \cos\theta_2}{\sin\left(\theta_1 - \theta_2\right)} \Big/ \dfrac{\mathrm{d}p}{\mathrm{d}t} = -\dfrac{1}{2\mu} \dfrac{\alpha^2}{\alpha^2 - \beta^2} \dfrac{\sqrt{gh}}{\sqrt{kh}\tanh kh} \left(-\dfrac{\beta^2}{\alpha^2} \tanh kh + 1 \right) + C_3 \dfrac{\sqrt{kh}}{\sqrt{\tanh kh}} & \text{(25a)} \\ \dfrac{a_v}{p} = \dfrac{g}{2\mu} \dfrac{\alpha^2}{\alpha^2 - \beta^2} \tanh kh. & \text{(25b)} \end{cases}$$

Note that the horizontal channels are rotated by an angle of $\theta_2 + \pi/2$ to eliminate other noise and obtain the wave noise. In the above equations, the left-hand sides can be calculated from original instrumental records, and the right-hand sides contain three parameters for inversion, that is, the shear modulus μ, the S-P velocity ratio β/α, and a kh-independent constant C_3. For continuous records of noise data, it is feasible to cut the data into small segments, stack the results of the left-hand sides, and perform a least-square search to find the best fit of the three parameters.

A preliminary attempt leads to unsatisfying results. Figure S3 in the supplementary information shows an example. The stacked results of the horizontal and vertical records seem to be very different from the theoretical form given by (25). As a result, the inversion suffers from large errors. We speculate that the reason is related to the assumption of uniform half-space model. A layered model is probably necessary to fit the

realistic data. Using a layered model, the first term of the right-hand side of equation (25a), and the right-hand side of equation (25b) can be calculated based on a numerical approach, leading to different dependences on kh. The second term of the right-hand side of equation (25a) does not change. Thus, the three inversion parameters are still μ, β/α and C_3. Again, the sensitivity and uncertainty of this method for layered structures should be tested in a future study. We point out that the vertical acceleration and pressure have been utilized for structure inversions in previous studies, mainly for low-frequency compliance noise in the deep ocean (e.g., Yamamoto & Torii, 1986; Crawford et al., 1998; Zha et al., 2014). The horizontal records have also been proposed for structure inversion, albeit ignoring the wave noise induced by wave forces (the second term of equation 25a) (Doran & Laske, 2016).

5 Noise removal

In the frequency range of interest (0.05−0.1 Hz), the horizontal and vertical noise induced by water waves can be removed using the pressure records, based on the fact that the horizontal acceleration is proportional to $\mathrm{d}p/\mathrm{d}t$, and the vertical acceleration is proportional to p. The ratio of the acceleration and the pressure in the frequency domain is called the pressure transfer function (PTF) (Crawford & Webb, 2000; Bell et al., 2015), that is, the horizontal PTF and vertical PTF are defined as

$$\begin{cases} \mathrm{HPTF}(f) = \dfrac{\mathrm{Fourier}\,(a_w)}{\mathrm{Fourier}\,(\mathrm{d}p/\mathrm{d}t)}, & \text{(26a)} \\ \mathrm{PTF}(f) = \dfrac{\mathrm{Fourier}\,(a_v)}{\mathrm{Fourier}\,(p)}. & \text{(26b)} \end{cases}$$

Note that the phase lag is ignored, which is theoretically zero.

Continuous noise data are first filtered between 0.05−0.1 Hz, and cut into small segments of 1,000 s. The two horizontal records are rotated to the perpendicular direction of other noise to totally eliminate other noise. In practice, the rotation is done by maximizing the correlation between channel 1 and $\mathrm{d}p/\mathrm{d}t$, which is equivalent to the perpendicular direction of other noise if the random noise is negligible (equation 18b). Channel 1 after rotation, $\mathrm{d}p/\mathrm{d}t$, channel z, and the pressure channel are Fourier transformed, and the horizontal and vertical PTFs are calculated according to equations (26). The PTFs are then averaged over a certain amount of time. To remove the noise in a data segment, the time derivative of the pressure and the pressure itself are Fourier transformed, and multiplied by the horizontal and vertical PTF, respectively, to predict the horizontal and vertical noise. The predicted noise is subtracted from the original data to extract the earthquake signals.

An example of the noise removal at station FN07A is shown in Figure 10. Data are from a Mw 5.6 earthquake that occurred at 04:14:00 on 13 October 2011. The epicenter is 43.46° N, 127.14° W, the focal depth is 20.6 km, and the hypocenter distance is about 3.78°. The original data are filtered between 0.05−0.1 Hz. The horizontal PTF is averaged over 12 hours, excluding a period of 2,000 s that contains the earthquake signals. The vertical PTF is averaged over the total recording period, which lasts about one year. The reason is that in practice it is found that the horizontal PTF changes more significantly over time than the vertical PTF, so it has to be averaged over a short period close the the earthquake. The denoising results are displayed in Figure 10, which shows that the signal-to-noise ratio (SNR) is improved effectively by removing the wave-induced noise.

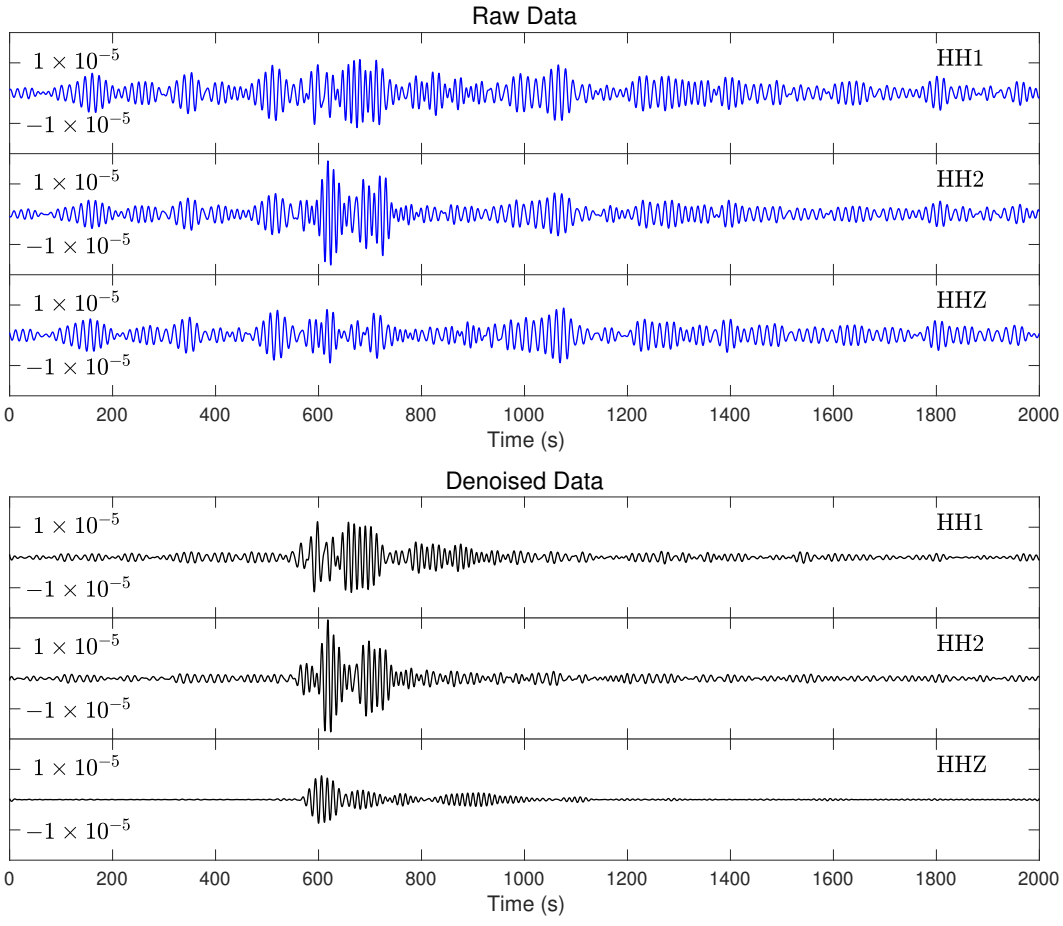

Figure 10. An example of removing the wave-induced noise at station FN07A. The data are filtered between 0.05−0.1 Hz. The top panel (blue) presents the raw recordings and the bottom panel (black) presents the results after noise removal.

The effectiveness of the noise removal for the horizontal records depends on the relative magnitude of the wave noise and other noise. Since the wave noise is proportional to $\mathrm{d}p/\mathrm{d}t$, it can be totally removed by using the horizontal PTF and the pressure records. Thus, if the water waves are strong at certain stations or during certain time periods, so that the wave noise dominates, the noise reduction is expected to be effective. At all of the 37 stations, typically a maximum reduction of 10−20 dB can be achieved. The PSDs before and after the noise removal during time periods of strong wave noise are given in Figure S4 in the supplementary information. After removing the wave noise, the dominant noise is other noise. The horizontal channels can be rotated to the direction of other noise to suppress other noise in the perpendicular direction, owing to the fact that other noise has a constant orientation (An et al., 2022). An example is shown in Figure S5 in the supplementary information. The noise removal of the vertical channel generally achieves satisfactory results, with noise reduction typically exceeding 20 dB (Figure S4), as the vertical records are dominated by compliance noise in this frequency range. We note that the vertical removal using the PTF method has been well developed by previous studies (Crawford & Webb, 2000; Bell et al., 2015; An et al., 2020).

6 Conclusion

In this study, we investigate the noise peak between 0.05−0.1 Hz at shallow-water stations ($<$ 300 m). We propose a noise model to explain the horizontal noise, which consists of three types of noise, the wave noise, other noise and background random noise. The wave noise is generated by two mechanisms, the seafloor deformation and the wave force. We demonstrate in theory that the wave noise is proportional to the time derivative of ocean-bottom pressure. The noise model and theory are verified to be consistent with realistic observations.

Two potential applications are discussed. First, the propagation direction of wave waters is derived. For all of the 27 stations, the wave propagation direction is always perpendicular to the coastline. Among them, at 25 stations the waves propagate from shallow water to deep sea. Second, the coefficient between the horizontal acceleration and the time derivative of the pressure (or the vertical acceleration) is used to constrain the underlying Earth structure. The inversion results are approximate, and could be improved by incorporating inversion models of layered structures. Finally, a denoising method is developed based on the noise model. The effectiveness of the noise removal depends on the relative magnitude of the wave noise and other noise, and at most stations, a maximum reduction of $10-20$ dB can be achieved for the horizontal channels.

Acknowledgments

This work made use of the GMT software (Wessel et al., 2019). This work is supported by the National Natural Science Foundation of China (NSFC) grant T2122012 and 42176073.

Data Availability

The OBS data used in this study are available through the IRIS Data Management Center (IRIS DMC).

References

An, C., Cai, C., Zheng, Y., Meng, L., & Liu, P. (2017). Theoretical solution and applications of ocean bottom pressure induced by seismic seafloor motion. *Geophysical Research Letters*, *44*(20).

An, C., Cai, C., Zhou, L., & Yang, T. (2022). Characteristics of low-frequency horizontal noise of ocean-bottom seismic data. *Seismological Research Letters*, *93*(1), 257–267.

An, C., & Liu, P. L. (2016). Analytical solutions for estimating tsunami propagation speeds. *Coastal Engineering*, *117*, 44–56.

An, C., Shawn Wei, S., Cai, C., & Yue, H. (2020). Frequency limit for the pressure compliance correction of ocean-bottom seismic data. *Seismological Research Letters*, *91*(2A), 967–976.

Araki, E., Shinohara, M., Sacks, S., Linde, A., Kanazawa, T., Shiobara, H., … Suyehiro, K. (2004). Improvement of seismic observation in the ocean by use of seafloor boreholes. *Bulletin of the Seismological Society of America*, *94*(2), 678–690.

Bell, S. W., Forsyth, D. W., & Ruan, Y. (2015). Removing noise from the vertical component records of ocean-bottom seismometers: Results from year one of the Cascadia Initiative. *Bulletin of the Seismological Society of America*, *105*(1), 300–313.

Bowden, D., Kohler, M. D., Tsai, V., & Weeraratne, D. S. (2016). Offshore Southern California lithospheric velocity structure from noise cross-correlation functions. *Journal of Geophysical Research: Solid Earth*, *121*(5), 3415–3427.

Cai, C., Wiens, D. A., Shen, W., & Eimer, M. (2018). Water input into the Mariana subduction zone estimated from ocean-bottom seismic data. *Nature*, *563*(7731), 389.

Crawford, W. C. (2004). The sensitivity of seafloor compliance measurements to sub-basalt sediments. *Geophysical Journal International*, *157*(3), 1130–1145.

Crawford, W. C., & Webb, S. C. (2000). Identifying and removing tilt noise from low-frequency (< 0.1 Hz) seafloor vertical seismic data. *Bulletin of the Seismological Society of America*, *90*(4), 952–963.

Crawford, W. C., Webb, S. C., & Hildebrand, J. A. (1991). Seafloor compliance observed by long-period pressure and displacement measurements. *Journal of Geophysical Research: Solid Earth*, *96*(B10), 16151–16160.

Crawford, W. C., Webb, S. C., & Hildebrand, J. A. (1998). Estimating shear velocities in the oceanic crust from compliance measurements by two-dimensional finite difference modeling. *Journal of Geophysical Research: Solid Earth*, *103*(B5), 9895–9916.

Dalrymple, R. A., & Dean, R. G. (1991). *Water wave mechanics for engineers and scientists*. Englewood Cliffs, New Jersey: World Scientific Publishing Company.

Deng, H., An, C., Cai, C., & Ren, H. (2022). Theoretical solution and applications of ocean bottom pressure induced by seismic waves at high frequencies. *Geophysical Research Letters*, *49*(9), e2021GL096952.

Doran, A., & Laske, G. (2016). Infragravity waves and horizontal seafloor compliance. *Journal of Geophysical Research: Solid Earth*, *121*(1), 260–278.

Doran, A., & Laske, G. (2017). Ocean-bottom seismometer instrument orientations via automated Rayleigh-wave arrival-angle measurements. *Bulletin of the Seismological Society of America*, *107*(2), 691–708.

Doran, A., & Laske, G. (2019). Seismic structure of marine sediments and upper oceanic crust surrounding Hawaii. *Journal of Geophysical Research: Solid Earth*, *124*(2), 2038–2056.

Doran, A., Rapa, M., Laske, G., Babcock, J., & McPeak, S. (2019). Calibration of differential pressure gauges through in situ testing. *Earth and Space Science*, *6*(12), 2663–2670.

Duennebier, F. K., Blackinton, G., & Sutton, G. H. (1981). Current-generated noise recorded on ocean bottom seismometers. *Marine Geophysical Researches*, *5*(1), 109–115.

Duennebier, F. K., & Sutton, G. H. (1995). Fidelity of ocean bottom seismic observations. *Marine Geophysical Researches*, *17*(6), 535–555.

Essing, D., Schlindwein, V., Schmidt-Aursch, M. C., Hadziioannou, C., & Stähler, S. C. (2021). Characteristics of current-induced harmonic tremor signals in ocean-bottom seismometer records. *Seismological Research Letters*, *92*(5), 3100–3112.

Herbers, T., Elgar, S., & Guza, R. (1995). Generation and propagation of infragravity waves. *Journal of Geophysical Research: Oceans*, *100*(C12), 24863–24872.

Janiszewski, H. A., Eilon, Z., Russell, J., Brunsvik, B., Gaherty, J., Mosher, S., … Coats, S. (2023). Broad-band ocean bottom seismometer noise properties. *Geophysical Journal International*, *233*(1), 297–315.

Janiszewski, H. A., Gaherty, J. B., Abers, G. A., Gao, H., & Eilon, Z. C. (2019). Amphibious surface-wave phase-velocity measurements of the Cascadia subduction zone. *Geophysical Journal International*, *217*(3), 1929–1948.

Peterson, J. (1993). *Observations and modeling of seismic background noise* (Tech. Rep.). Albuquerque, New Mexico, USA: U.S. Department of Interior Geological Survey.

Reddy, T. R., Dewangan, P., Arya, L., Singha, P., & Raju, K. A. K. (2020). Tidal triggering of the harmonic noise in ocean-bottom seismometers. *Seismological Research Letters*, *91*(2A), 803–813.

Romanowicz, B., Stakes, D., Montagner, J. P., Tarits, P., Uhrhammer, R., Begnaud, M., … others (1998). MOISE: A pilot experiment towards long term sea-floor geophysical observatories. *Earth, planets and space*, *50*, 927–937.

Sheehan, A. F., Gusman, A. R., Heidarzadeh, M., & Satake, K. (2015). Array observations of the 2012 Haida Gwaii tsunami using Cascadia Initiative absolute and differential seafloor pressure gauges. *Seismological Research Letters*, *86*(5), 1278–1286.

Stähler, S. C., Schmidt-Aursch, M. C., Hein, G., & Mars, R. (2018). A self-noise model for the German DEPAS OBS pool. *Seismological Research Letters*, *89*(5), 1838–1845.

Sutton, G. H., & Duennebier, F. K. (1987). Optimum design of ocean bottom seismometers. *Marine geophysical researches*, *9*(1), 47–65.

Toomey, D. R., Allen, R. M., Barclay, A. H., Bell, S. W., Bromirski, P. D., Carlson, R. L., … others (2014). The Cascadia Initiative: A sea change in seismological studies of subduction zones. *Oceanography*, *27*(2), 138–150.

Trehu, A. (1985). A note on the effect of bottom currents on an ocean bottom seismometer. *Bulletin of the Seismological Society of America*, *75*(4), 1195–1204.

Webb, S. C. (1988). Long-period acoustic and seismic measurements and ocean floor currents. *IEEE Journal of Oceanic Engineering*, *13*(4), 263–270.

Webb, S. C. (1998). Broadband seismology and noise under the ocean. *Reviews of Geophysics*, *36*(1), 105–142.

Webb, S. C., & Crawford, W. C. (2010). Shallow-water broadband OBS seismology. *Bulletin of the Seismological Society of America*, *100*(4), 1770–1778.

Wei, S. S., Wiens, D. A., Zha, Y., Plank, T., Webb, S. C., Blackman, D. K., … Con-

563 der, J. A. (2015). Seismic evidence of effects of water on melt transport in the
564 Lau back-arc mantle. *Nature*, *518*(7539), 395.
565 Wessel, P., Luis, J., Uieda, L., Scharroo, R., Wobbe, F., Smith, W., & Tian, D.
566 (2019). The generic mapping tools version 6. *Geochemistry, Geophysics, Geosys-*
567 *tems*, *20*(11), 5556–5564.
568 Wu, Y., Yang, T., Liu, D., Dai, Y., & An, C. (2023). Current-induced noise in ocean
569 bottom seismic data: Insights from a laboratory water flume experiment. *Earth*
570 *and Space Science*, *10*(6), e2022EA002531.
571 Yamamoto, T., & Torii, T. (1986). Seabed shear modulus profile inversion using
572 surface gravity (water) wave-induced bottom motion. *Geophysical Journal Inter-*
573 *national*, *85*(2), 413–431.
574 Zha, Y., & Webb, S. C. (2016). Crustal shear velocity structure in the Southern Lau
575 basin constrained by seafloor compliance. *Journal of Geophysical Research: Solid*
576 *Earth*, *121*(5), 3220–3237.
577 Zha, Y., Webb, S. C., Nooner, S. L., & Crawford, W. C. (2014). Spatial distribu-
578 tion and temporal evolution of crustal melt distribution beneath the East Pacific
579 Rise at 9° − 10° N inferred from 3-D seafloor compliance modeling. *Journal of*
580 *Geophysical Research: Solid Earth*, *119*(6), 4517–4537.

Figure 1.

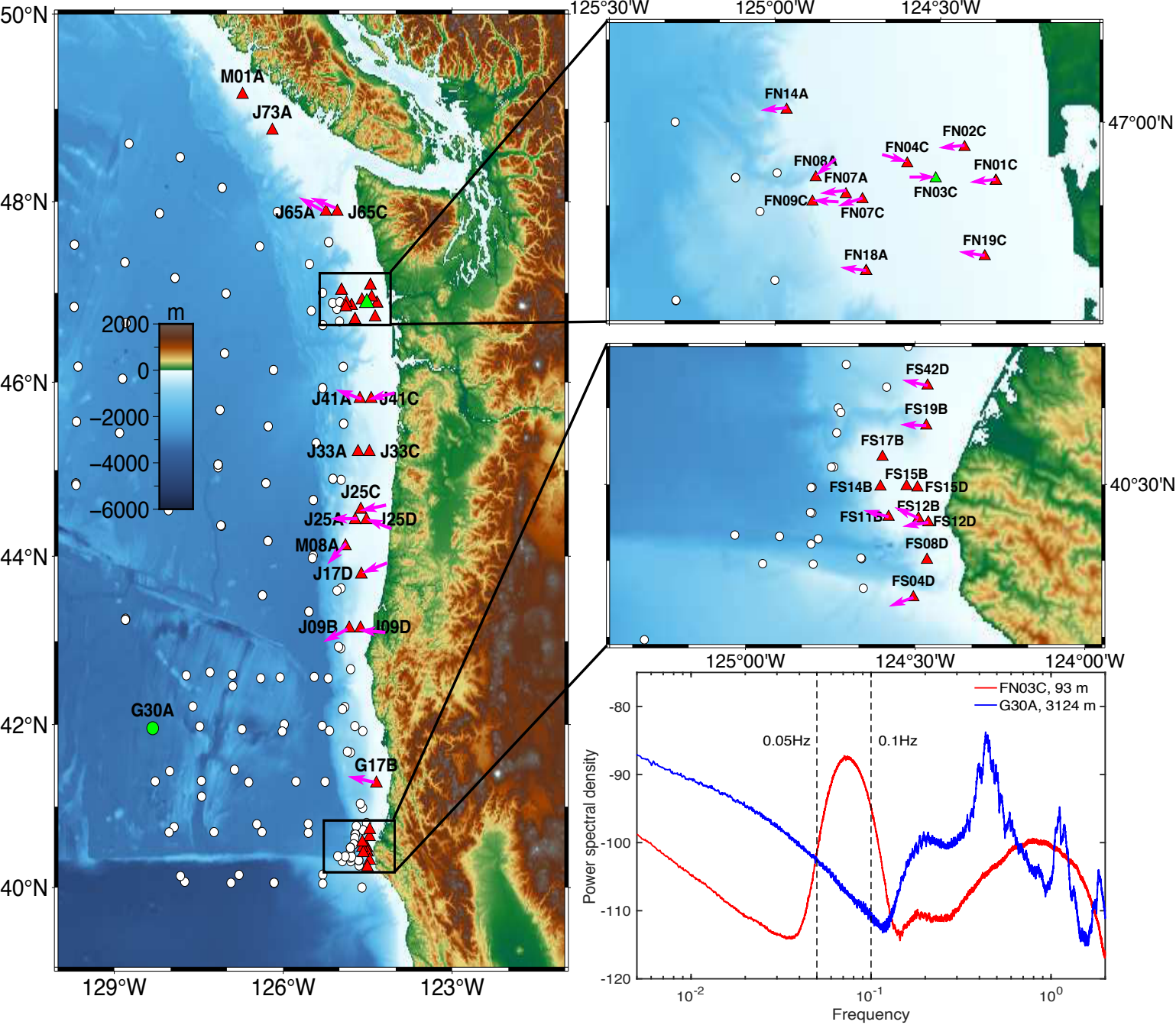
M01A
J73A
J65A
J65C
J41A
J41C
J33A
J33C
J25C
J25A
J25D
M08A
J17D
J09B
J09D
G30A
G17B
m
2000
0
−2000
−4000
−6000
50°N
48°N
46°N
44°N
42°N
40°N
129°W
126°W
123°W
125°30'W
125°00'W
124°30'W
47°00'N
FN14A
FN02C
FN04C
FN08A
FN01C
FN07A
FN03C
FN09C
FN07C
FN19C
FN18A
40°30'N
FS42D
FS19B
FS17B
FS15B
FS14B
FS15D
FS12B
FS11B
FS12D
FS08D
FS04D
124°00'W
FN03C, 93 m
G30A, 3124 m
0.05Hz
0.1Hz
Power spectral density
-80
-90
-100
-110
-120
10^{-2}
10^{-1}
10^{0}
Frequency

Figure 2.

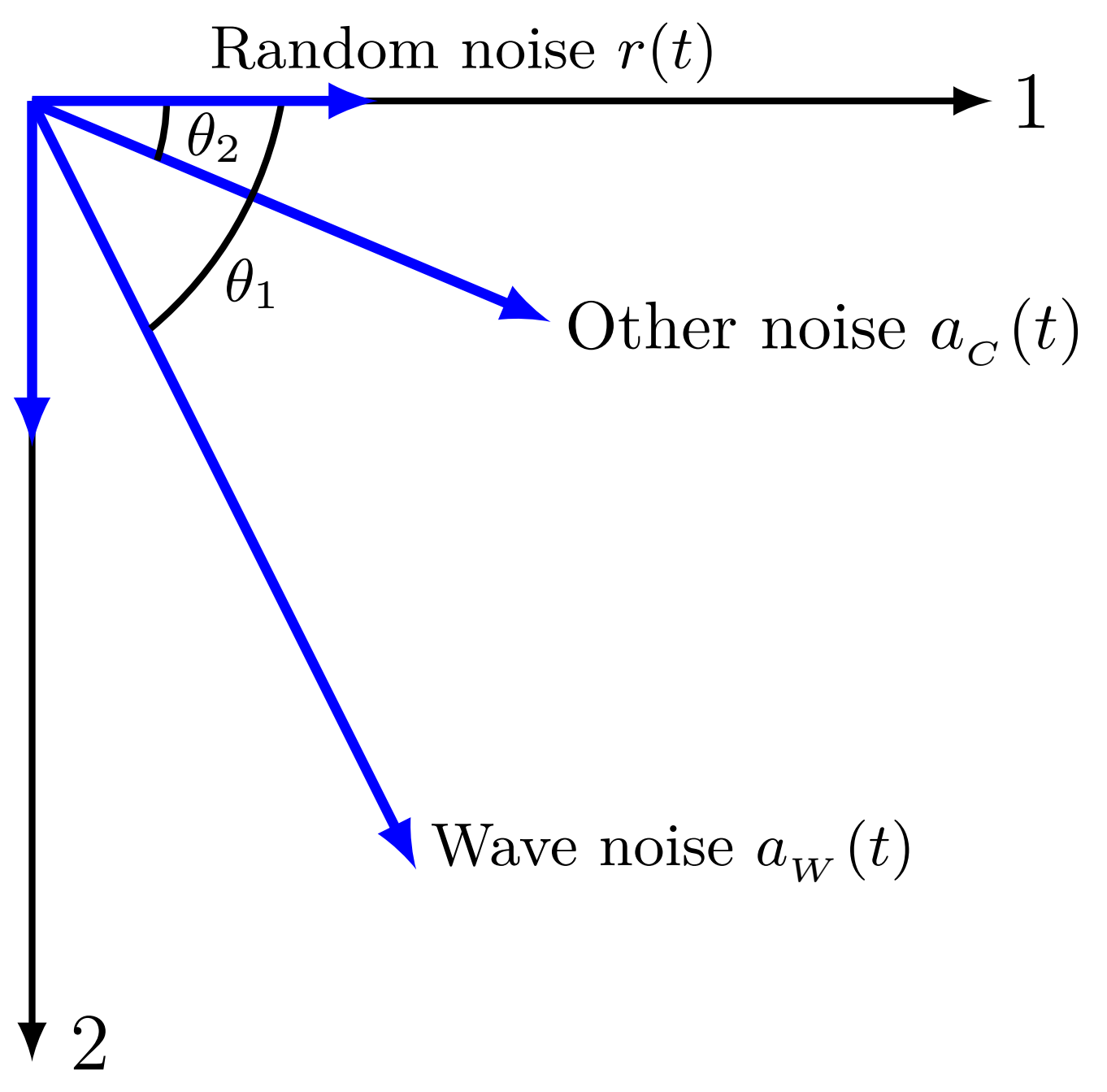
Random noise $r(t)$
1
θ_2
θ_1
Other noise $a_C(t)$
Wave noise $a_W(t)$
2

Figure 3.

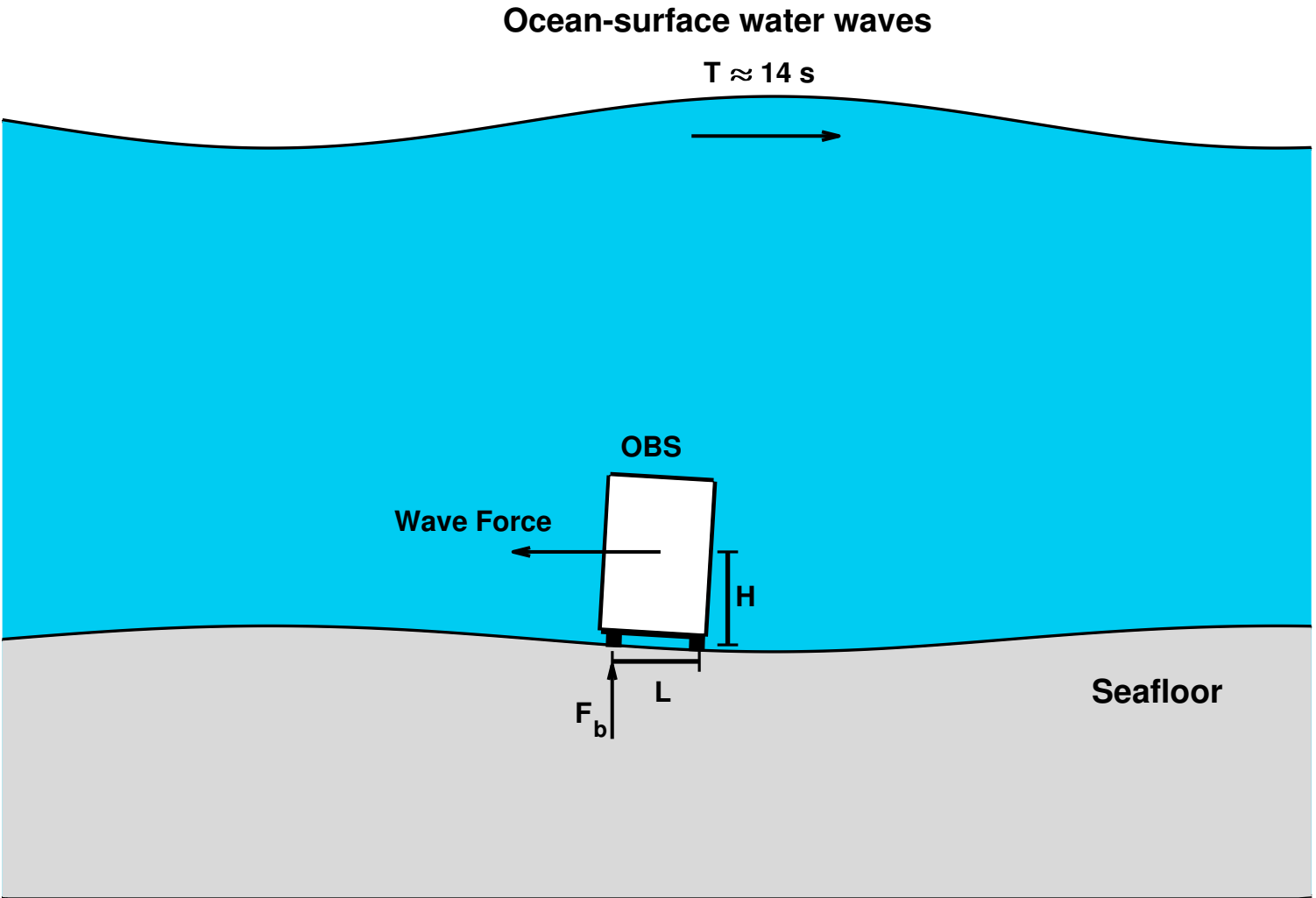
Ocean-surface water waves
T ≈ 14 s
OBS
Wave Force
H
L
F b
Seafloor

Figure 4.

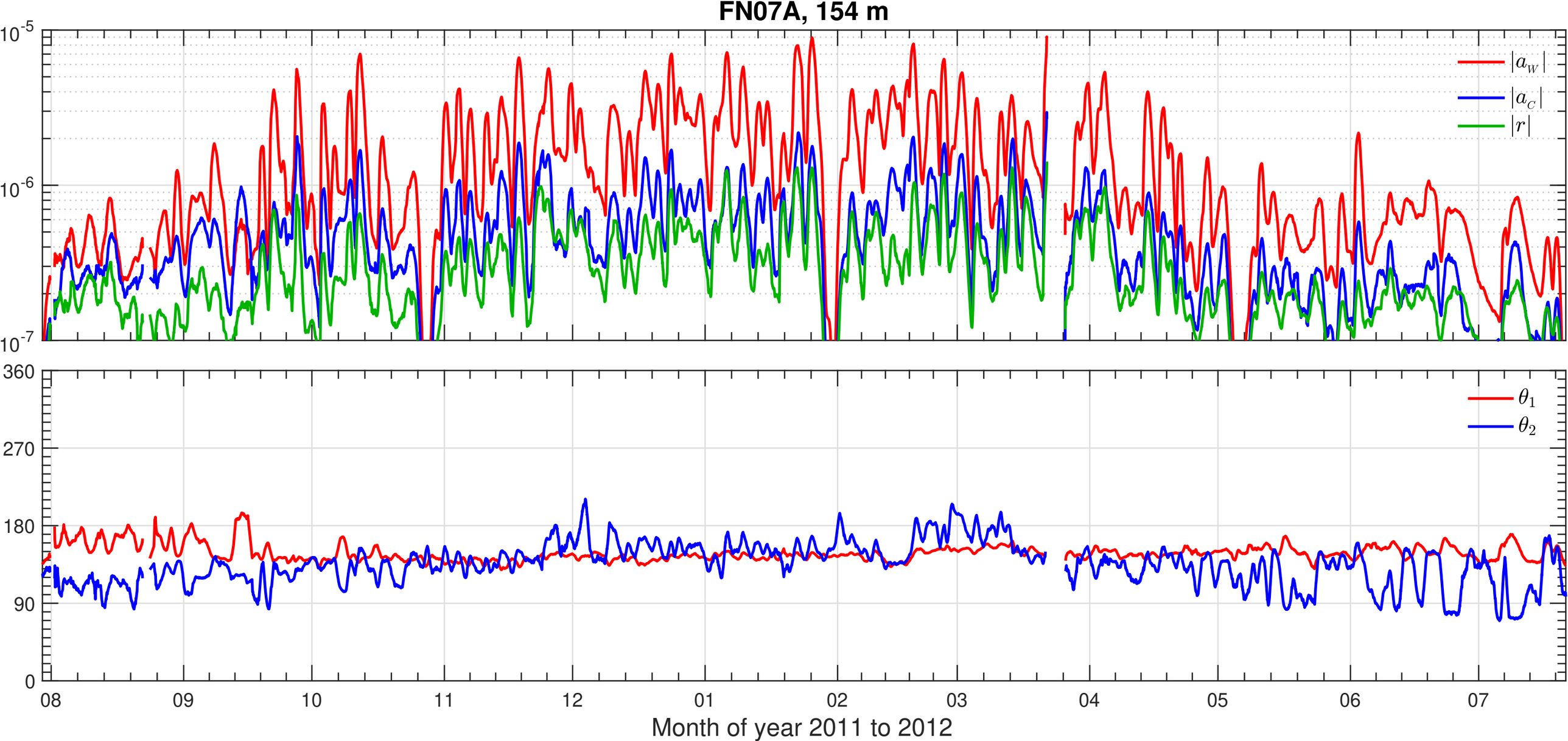
FN07A, 154 m
10^{-5}
10^{-6}
10^{-7}
$|a_W|$
$|a_C|$
$|r|$
360
270
180
90
0
θ_1
θ_2
08
09
10
11
12
01
02
03
04
05
06
07
Month of year 2011 to 2012

Figure 5.

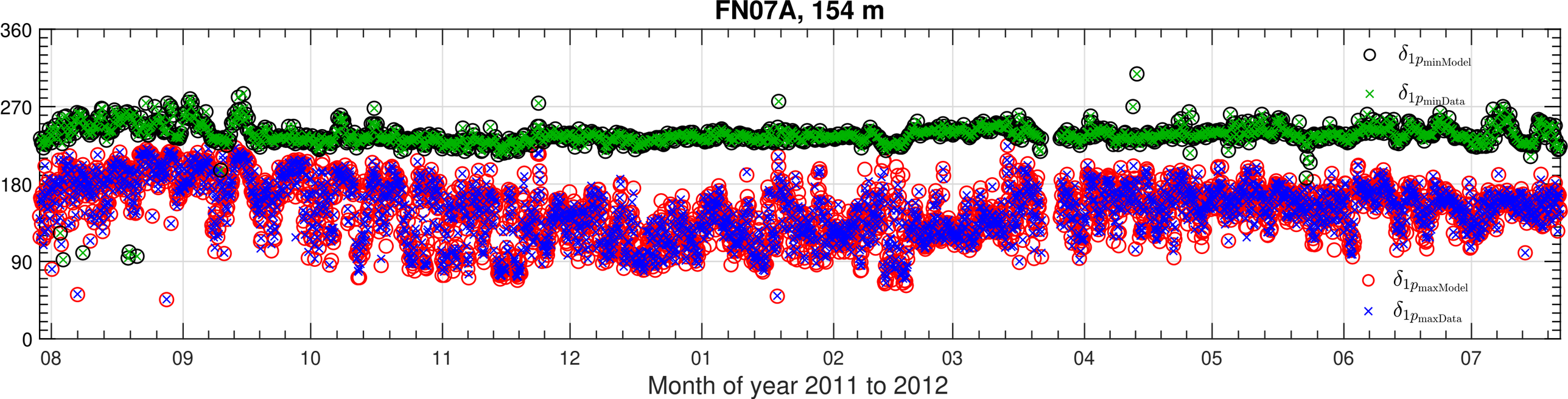
FN07A, 154 m
360
270
180
90
0
08
09
10
11
12
01
02
03
04
05
06
07
Month of year 2011 to 2012
$\delta_{1p_{\mathrm{minModel}}}$
$\delta_{1p_{\mathrm{minData}}}$
$\delta_{1p_{\mathrm{maxModel}}}$
$\delta_{1p_{\mathrm{maxData}}}$

Figure 6.

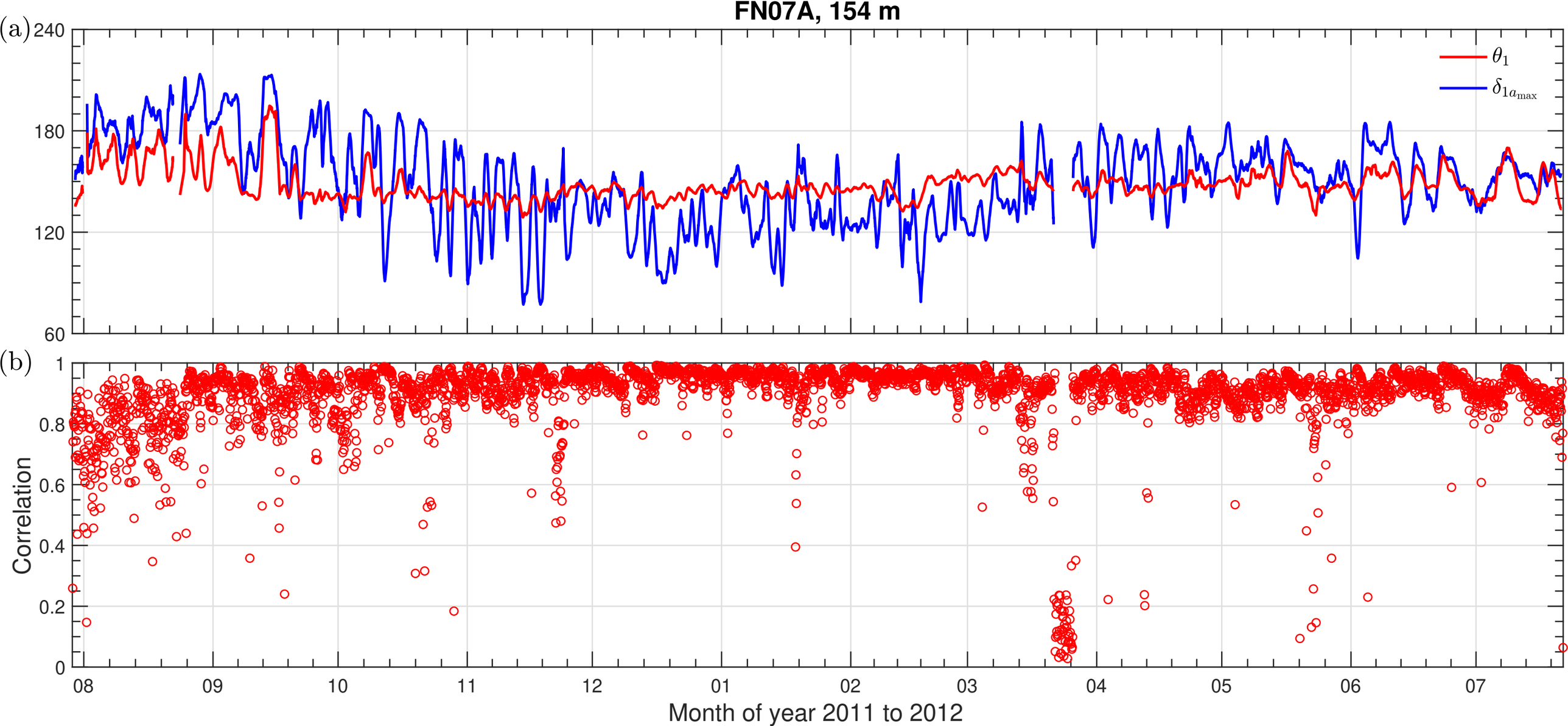
FN07A, 154 m
(a)
240
180
120
60
θ_1
$\delta_{1a_{\max}}$
(b)
Correlation
1
0.8
0.6
0.4
0.2
0
08
09
10
11
12
01
02
03
04
05
06
07
Month of year 2011 to 2012

Figure 7.

FN03C, 93 m

(a)

150
90
30
-30

θ_1
θ_2

(b)

1
0.8
0.6
0.4
0.2
0

Correlation

10
11
12
01
02
03
04
05
06

Month of year 2013 to 2014

(c)

$\times 10^{-5}$

5
-5

Noise

$\frac{\mathrm{dp}}{\mathrm{dt}} \times -1.18 \times 10^{-7} \mathrm{m/s^2} \cdot \frac{\mathrm{s}}{\mathrm{Pa}}$

$a_1 \cos\theta_1 + a_2 \sin\theta_1$

OT = 2014-01-29 05:13:20

0
200
400
600
800
1000

Time (s)

Figure 8.

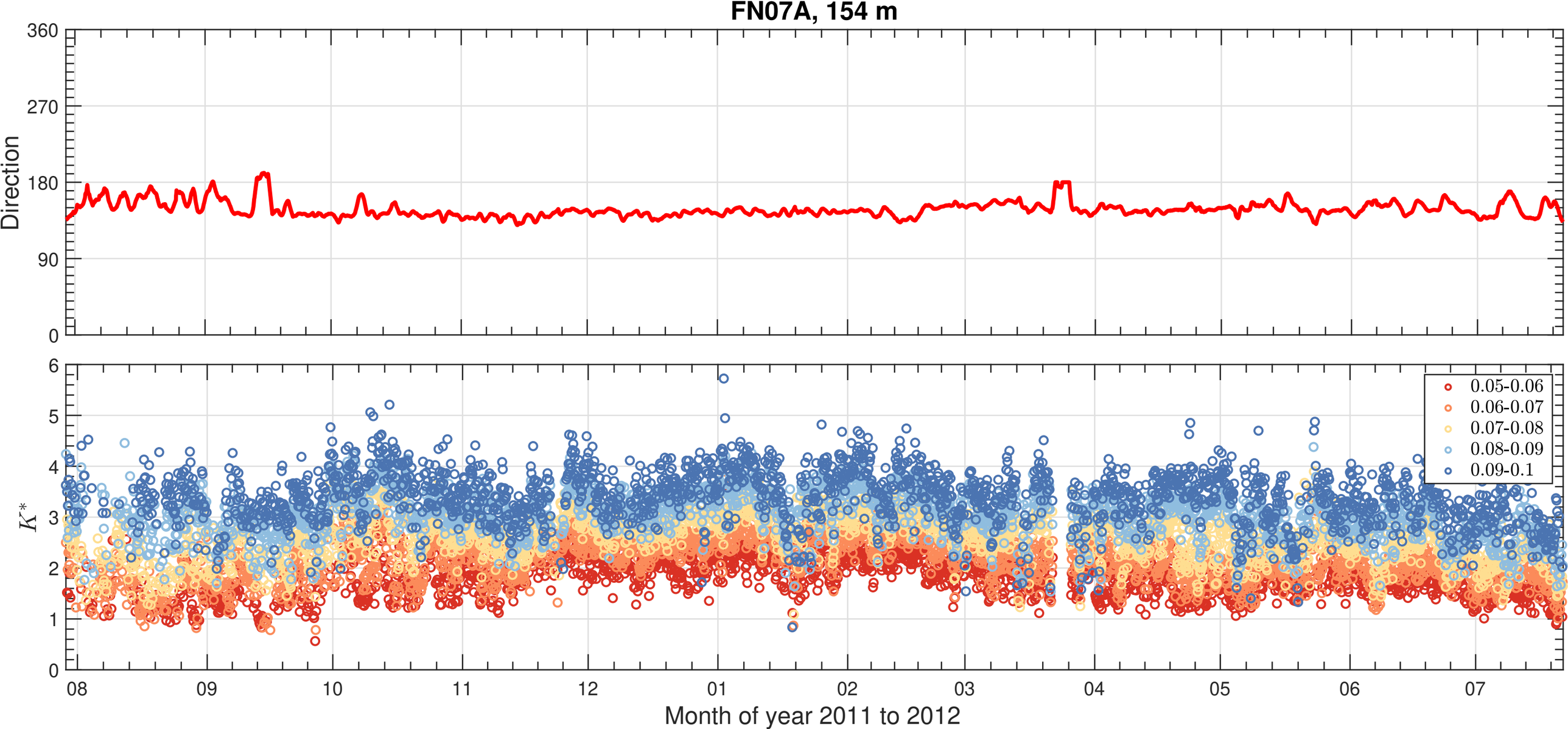
FN07A, 154 m
Direction
360
270
180
90
0
K^*
6
5
4
3
2
1
0
0.05-0.06
0.06-0.07
0.07-0.08
0.08-0.09
0.09-0.1
08
09
10
11
12
01
02
03
04
05
06
07
Month of year 2011 to 2012

Figure 9.

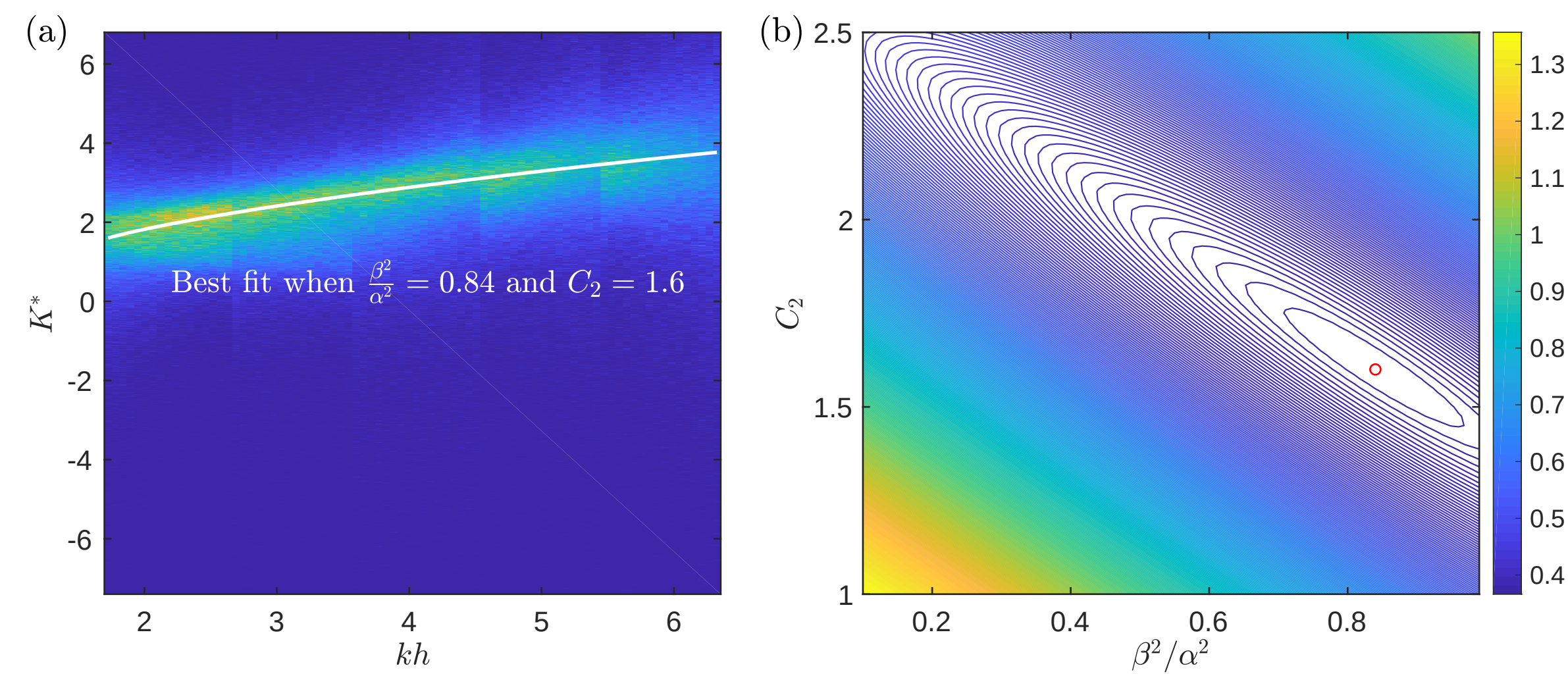
(a)
Best fit when $\frac{\beta^2}{\alpha^2} = 0.84$ and $C_2 = 1.6$
K^*
kh
6
4
2
0
-2
-4
-6
2
3
4
5
6
(b)
C_2
β^2/α^2
2.5
2
1.5
1
0.2
0.4
0.6
0.8
1.3
1.2
1.1
1
0.9
0.8
0.7
0.6
0.5
0.4

Figure 10.

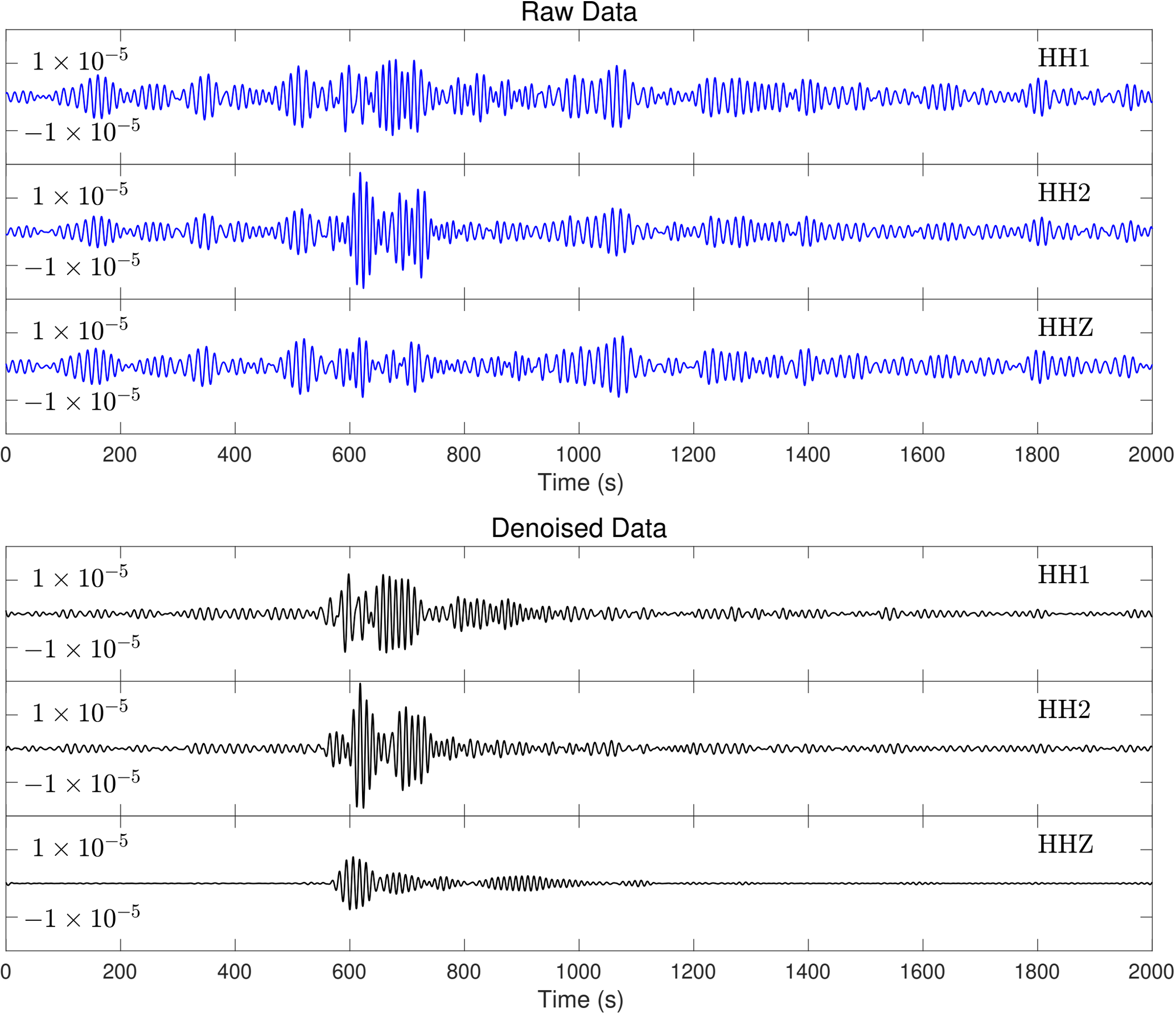
Raw Data
1×10^{-5}
-1×10^{-5}
HH1
HH2
HHZ
0
200
400
600
800
1000
1200
1400
1600
1800
2000
Time (s)
Denoised Data
1×10^{-5}
-1×10^{-5}
HH1
HH2
HHZ
0
200
400
600
800
1000
1200
1400
1600
1800
2000
Time (s)